# The Impact of Graphene Sheet Size on the Performance of Interconnected Graphene Foam-Based Supercapacitors

by

Serubbabel Sy

A thesis

presented to the University of Waterloo

in fulfillment of the

thesis requirement for the degree of

Master of Applied Science

in

Chemical Engineering

Waterloo, Ontario, Canada, 2015

# Author's Declaration

I hereby declare that I am the sole author of this thesis. This is a true copy of the thesis, including any required final revisions, as accepted by my examiners.

I understand that my thesis may be made electronically available to the public.

# Abstract

The increasing demand for energy and growing concerns of propagating greenhouse emissions has directed many investments towards the furtherance of benign energy storage commercialization. Unfortunately, batteries continue to maintain their dominance on the markets of vehicles, and portable electronics. Supercapacitors, however, have actually recently started carving out market shares in these two areas. Supercapacitors can be found complementing existing technology, and in some cases replacing battery powered devices. The major of advantage of utilizing oil as the primary energy source lies in its ability to conjure large amounts of energy in short amounts of time. This is another niche market that supercapacitors can establish for itself: supplying moderate energy storage but capable of large bursts when necessary.

A derivative of carbon called graphene has also been at the forefront of many research fields. The pace of graphene research has escalated quickly within the past decade, especially after Geim and Novoselov introduced the "scotch-tape method" of obtaining monolayer graphene. Graphene is a two-dimensional $sp^2$ honeycomb allotrope of carbon that exhibit amazing optical, electrical, thermal, electrical and mechanical properties. Although many scientists have discovered many creative ways of producing graphene-based products, some fundamental properties remain a mystery.

Herein, this proposed work was directed at affirming the relationship between the lateral graphene sheet size and its effect on graphene foam-based supercapacitors. For this, two graphene oxide (GO) materials produced from two different graphite precursors, were deposited into porous nickel and then chemically reduced in-situ. Subsequently, these electrodes were lyophilized and fabricated into a coin cell supercapacitor. These foam devices prepared with smaller planar graphene sheets exhibited 3-16% higher gravimetric capacitance than those prepared with larger sheets. These differences in performance was likely resulted from the higher surface area, lower ion transport resistance and improved ionic wettability

inherent to graphene with smaller sheets. However, impedance characterizations has shown that larger graphene sheets possess higher electrical conductivity than that of smaller graphene sheets.

It is believed this work will provide some guidance when tailoring the graphene planar sheet size depending on the situation and application. This work may also find use in other energy applications such as electrolyte development, fuel cells and batteries.

# Acknowledgements

Special thanks goes to my supervisor, Dr. Aiping Yu and several of my colleagues including Salah Abureden, Victor Chabot, Brian Hsu, Gregory Liu, Drew Higgins, Ja-Yeon Choi, Kun Feng, Gaopeng Jiang, and Hadis Zarrin for their assistance and support.

I also want to thank Dr. Zhongwei Chen for providing additional equipment and lab space to perform my experiment.

I would also like to acknowledge the support from my committee including: Dr. Aiping Yu, Dr. Boxin Zhao, and Dr. Michael Pope

# Table of Contents

# List of Figures

# List of Tables

# List of Abbreviations, Symbols and Nomenclature

A                       Absorbance

AA                      Ascorbic Acid

BET (theory)            Brunauer-Emmett-Teller theory, describes adsorption of gas molecules

c                       BET constant

C                       Capacitance

$C_0$                   Initial Concentration

$C_e$                   Equilibrium Concentration

$C_S$                   Specific Capacitance: capacitance normalized by mass

CNT                     Carbon nanotubes

CV                      Cyclic Voltammetry

CVD                     Chemical vapor deposition

d                       lattice/interplanar spacing

DSC                     Differential scanning calorimetry

EDA                     Ethylenediamine

EDLC                    Electric double-layer capacitors

EIS                     Electrochemical Impedance Spectroscopy

ESR                     Equivalent series resistance

GO                      Graphene Oxide

| GCD | Galvanostatic Charge Discharge |
| --- | --- |
| GQD | Graphene quantum dots |
| I | current |
| $I_D$ | Intensity of D-peak |
| $I_G$ | Intensity of G-peak |
| IR drop | Voltage drop |
| OECD | Organization for Economic Cooperation and Development |
| L | Length of path |
| L-graphite | Graphite (large, flake) |
| L-GO | Graphene Oxide (oxidized from L-graphite) |
| L-rGO | Reduced graphene oxide (reduced from L-GO) |
| $L_a$ | Interdefect distance |
| M, m | Mass |
| MB | Methylene blue |
| MWCNT | Multi-walled carbon nanotubes |
| NMR | Nuclear magnetic resonance |
| R | Resistance (R) |
| Redox | Reduction and oxidization |
| rGO | Reduced graphene oxide |
| $R_S$ | Ohmic Resistance |

| | |
|---|---|
| s-graphite | graphite (small, powder) |
| s-GO | Graphene oxide (oxidized from s-graphite) |
| s-rGO | Reduced graphene oxide (reduced from s-GO) |
| SEM | Scanning Electron Microscope |
| TEM | Transmission Electron Microscope |
| TGA | Thermogravimetric analysis |
| UV | Ultraviolet |
| UV-Vis | Ultraviolet-Visible: pertaining to the spectrum that is encompassed |
| V | Volume |
| XRD | X-ray Diffraction |
| Zim | Impedance (imaginary resistance) |
| Zre | Resistance (real resistance) |
| $\varepsilon$ | molar extinction coefficient |
| $\theta$ | diffraction angle |
| $\lambda$ | wavelength (of light and raman laser) |
| $\omega$ | Frequency |

# 1.0   Introduction

With the increasing hunger for energy, yet simultaneous need to shrink the carbon footprint, the demand for environmentally friendly, sustainable energy has been the forefront of modern-day research.
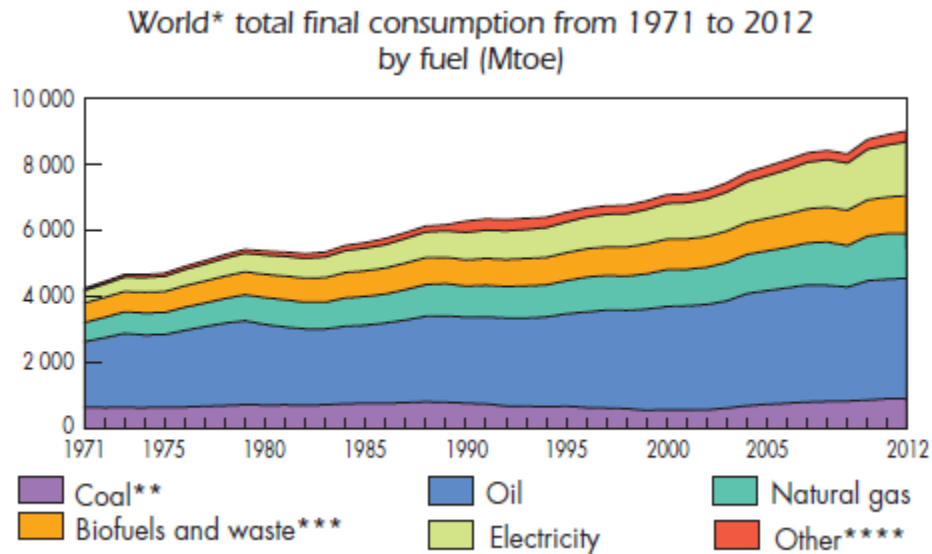


**Figure 1. Graphical representation of World Energy Consumption © OECD/IEA 2013 World Energy Outlook, IEA Publishing.**[1]

As published from OECD (Figure 1), the upward consumption of fuel has not slowed down since 1971.[1] The breakdown of energy consumption is prevalently dominated by oil followed by electricity. On the other side of the market, the dwindling supply of fossil fuel reserves and natural gas has added much pressure to develop alternative energy sources. Lastly and unfortunately, the development of energy storage and power supply technology has been rather slow compared to other technologies. All these factors consummate into a relentless impetus to invest into the research of alternative energy sources.
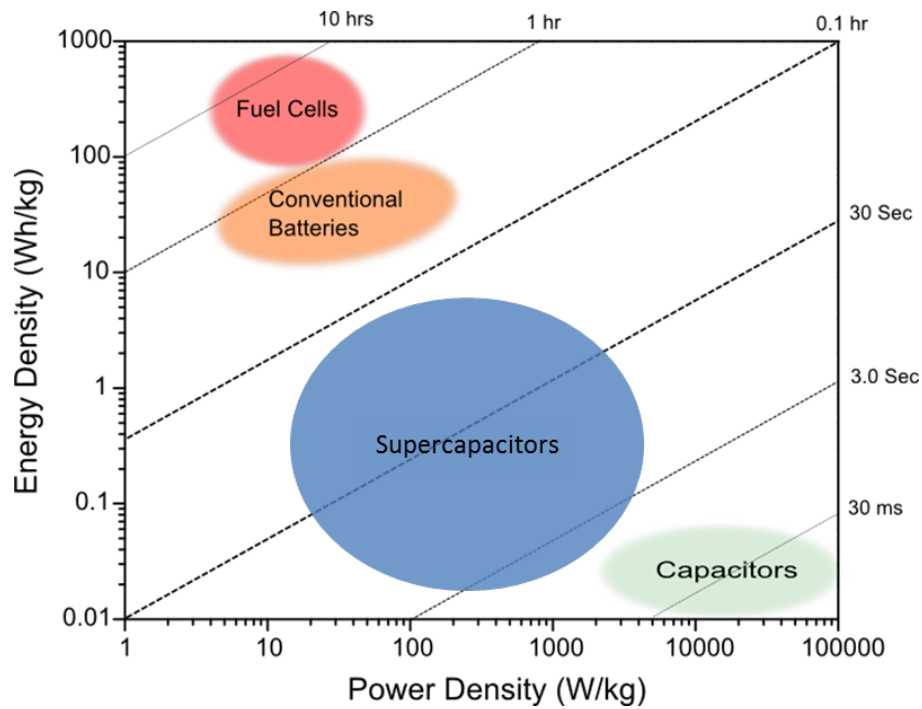
**Figure 2. Ragone Plot depicting common sources of energy storage**

Figure 2 depicts the Ragone plot outlining where modern energy storage devices would balance between energy density and power density. For this purpose, the ideal energy storage device should possess both high power and energy densities. Other important characteristics include (but not limited to): high, stable cyclability, environmentally benign, and fast charging. One technology of interest is the supercapacitor, which is an energy storage that delivers short but large bursts of power, however, unfortunately lacks the high energy density to sustain long periods of discharge. Supercapacitors has already begun to pervade the industry, often seen complementing existing technologies. Supercapacitor electrodes are often prepared with a carbon derivative, due to its high surface area.

The $sp^2$-planar derivative of carbon, graphene, has been a strong focus of research recently. Graphene has begun to be implemented in a wide variety of applications, due to its amazing electrical, thermal, optical, and mechanical properties. However, there is still much hidden potential that still needs to be uncovered.

It is for these reasons that graphene will also be the primary material of focus within this thesis. There are many characteristics of graphene that can be manipulated to for energy storage purpose.

The objective of this thesis is to investigate the process of reduced graphene oxide synthesis, as well as supercapacitor assembly. However, the focus will be narrowed towards unravelling two characteristics of graphene, i.e. (i) graphene planar size (ii) amount of reduced graphene oxide foam and their effects on capacitance retention within supercapacitors.

## 1.1    Thesis Organization

This dissertation focuses on the development of graphene, graphene oxide and reduced graphene oxide synthesis as well as a brief snapshot on current supercapacitor technology. In section 2, a brief overview and literature review of the operating principles behind supercapacitors is covered, highlighting their advantages and deficits as energy storage devices. The background and brief development of the synthesis of graphene oxide and graphene is also covered in this section. Section 3 provides a brief description of the principal characterization techniques. Section 4 provides a detailed description of my progression in synthesizing graphene oxide and reduced graphene oxide as well as the results of my investigations. Lastly, Section 5 concludes my thesis in summarizing the thesis as well as potential venues that should be considered for future development.

# 2.0   Background

## 2.1   Supercapacitors

Supercapacitors, also known as ultracapacitors or double-layer capacitors, have attracted much attention since its inception in the 1950s.[2]  Recently, supercapacitors have pervaded various markets due to its high power density, low charge leakage, rapid charge and discharging and cycling stability. As examples within consumer electronics, supercapacitors are beginning to power LED flashlights,[3] Bluetooth speakers,[4] and portable power tools.[5] Within the transport industry, supercapacitors are being utilized in emergency doors, regenerative braking,[6] and even as the primary source of power on certain railcars.[7, 8] Supercapacitors are primarily comprised of two electrodes and an electrolyte in between, which electrically separates the two electrodes and facilitate ion transfer. Supercapacitors are subdivided primarily into 2 types: electric double-layer capacitors and pseudocapacitors.

### 2.1.1   Electric Double-layer Capacitors (EDLC)
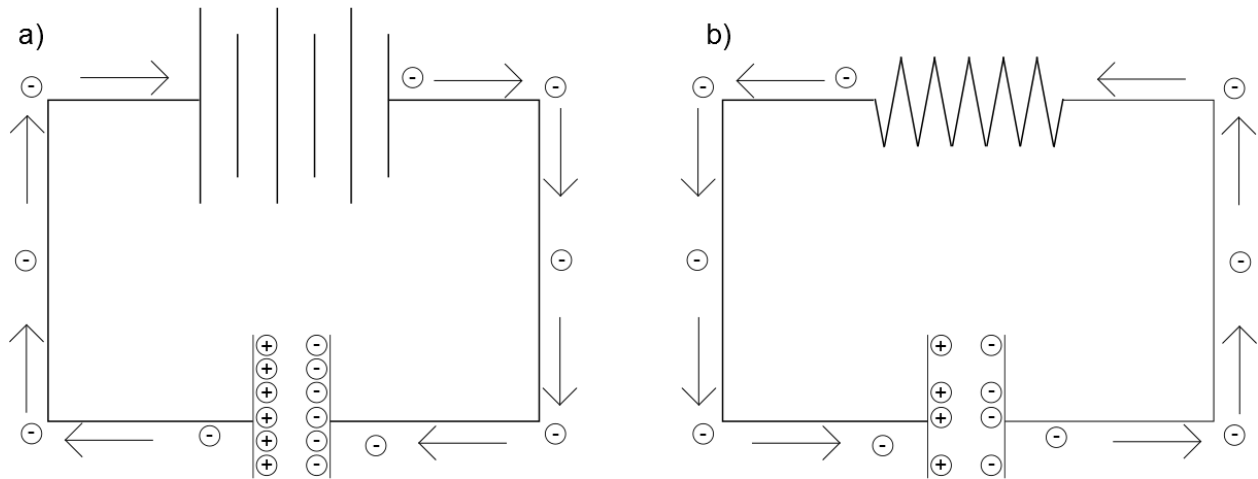


Figure 3. Schematic of charge and discharge of a conventional capacitor

4

Electric double-layer capacitors (EDLC) are also known as non-faradaic supercapacitors. These differ from conventional capacitors by which it stores far more capacitance. From Figure 2, supercapacitors possess larger energy density at the cost of some power density when compared to capacitors. When an energy source is connected to a capacitor (Figure 3 (a)), the electrons will flow from one plate through the energy source and into the other plate accumulating a potential difference between the plates. Here, the charge is stored via the electrostatic accumulation. Capacitor electrodes are typically insulated by air. When the energy source is replaced with a load (Figure 3 (b)) the potential difference dissipates, flowing electrons from the anode through the load into the cathode until the electrodes are potentially, at equilibrium.
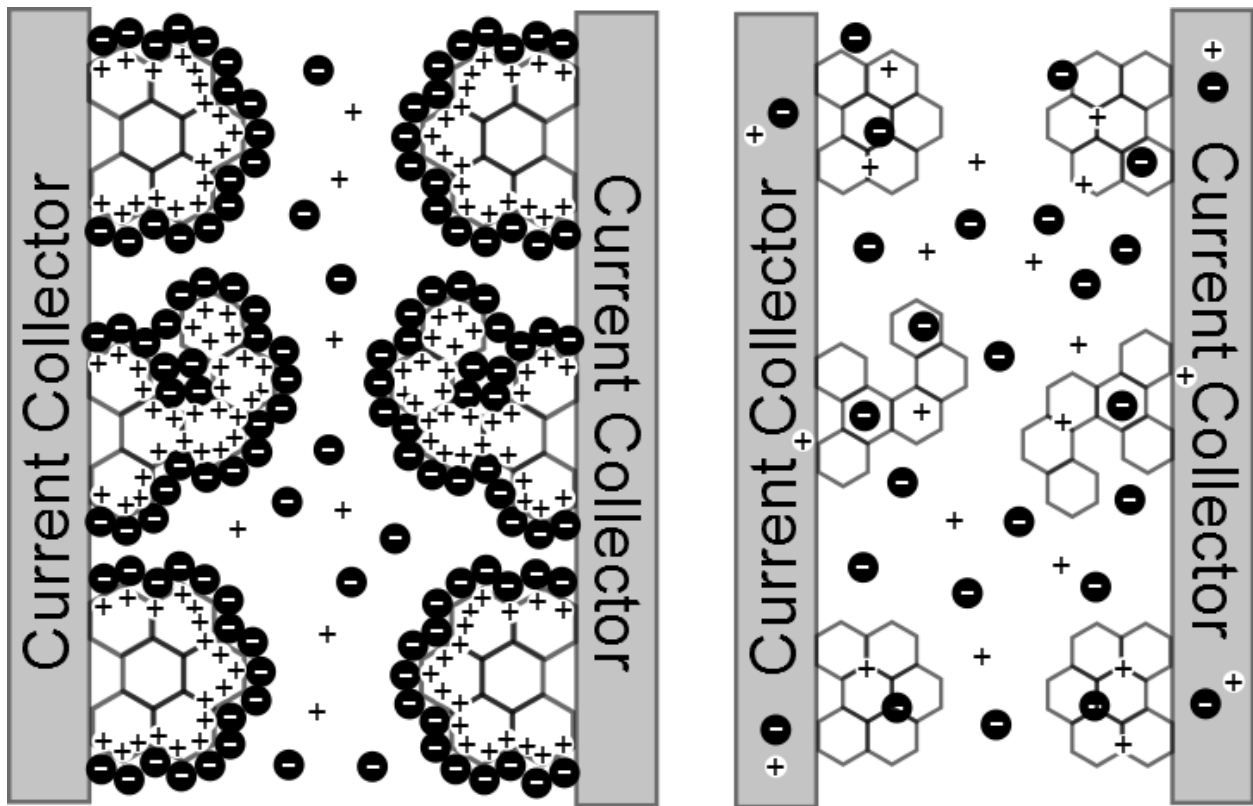


**Figure 4. Diagram of electrostatic accumulation of Double layer capacitors**

When an energy source is connected to an EDLC, it behaves similarly in that electrostatic accumulation occurs at the surface of each electrode. Although capacitor electrodes are generally flat metal plates, supercapacitors utilize some derivative of carbon or carbon composite deposited onto each electrode to serve as the electroactive material (Figure 4). A derivative or composite of carbon is commonly used due to carbon's chemical stability and high surface area, which translate to more area for electrostatic accumulation. Another major difference in the composition between capacitors and supercapacitors is the separator. Unlike conventional capacitors, supercapacitors are separated by electrolyte. These were typically ionic conductive liquids, however recently, solid membranes have also garnered much interest. Solid membranes were commonly polymers that were functionalized with ionic groups to double in function as separators and ionic conductors. Supercapacitor electrolyte can be divided into several categories:[9]

    I.     Aqueous (ex. KOH, KCl, $H_2SO_4$)

    II.     Organic (ex. $TEABF_4$/ACN)

    III.     Ionic-liquid ([EMIM][$BF_4$])

    IV.     Solid-state or quasi-solid-state. This category can be further subdivided into: dry solid polymer electrolyte, gel polymer electrolyte, inorganic electrolyte.

    V.     Redox-active electrolytes. This category overlaps with categories (I – III) with special emphasis on compounds that are redox-active

Unfortunately, supercapacitor's primary hindrance to ubiquitous commercialization lies in its limited energy density. Most of the research invested in supercapacitors has been tailored towards increasing the energy density. The primary methods to improving the energy density are as follows:

    I.     Increasing active surface area (ex. manipulating the electrode architecture)

    II.     Electrode/electrolyte compatibility (ex. adjusting surface functionality, pore structure/size, ion size, ion wettability)

III.     Introduce electrochemically active materials (ex. Redox reactions)

IV.     Increasing the operational voltage (ex. Utilizing non-aqueous electrolyte)

Of the two categories of supercapacitors, EDLCs will be focused upon within this thesis. The effects of pseudocapacitance will be considered negligible in this study, as will be justified in Section 5.

## 2.1.2    Faradaic Supercapacitors
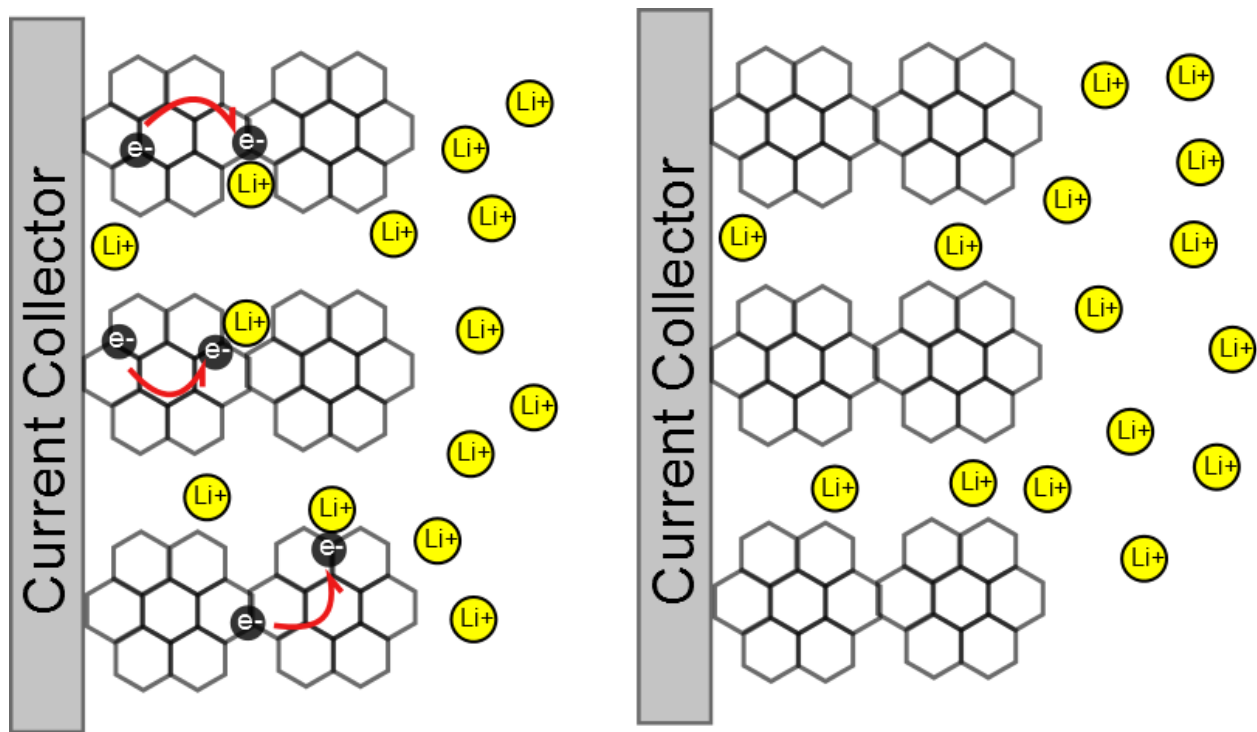


**Figure 5. Diagram of Li-ion intercalation in Faradaic supercapacitors**

Faradaic supercapacitors, also known as pseudocapacitors, undergo fast reversible faradaic (redox) reactions occur at each electrode when a potential is applied. Unlike EDLC, electro-activity is not limited to the surface, but rather, redox reactions can occur throughout the electrode. There are primarily 3 types of faradaic supercapacitors:

I.     Reversible adsorption (ex. Li-ion intercalation into graphene in Figure 5)[10]

II.     Redox reactions of transitional metal oxides (ex. RuO, MnO)[10, 11, 12, 13]

III.     Reversible electrochemical doping/dedoping within conductive polymers (ex. Polypyrrole, polyaninline)[14, 15]

Some faradaic capacitors are able to extend the working voltage and increase the energy density. Pseudocapacitors are similar to batteries in that pseudocapacitors usually retain larger amounts of capacitance and thereby possess larger energy densities. Pseudocapacitors carry relatively lower power densities compared to EDLCs by cause of slower charging and discharging. The process of redox reactions occur naturally slower than electrostatic accumulation. Pseudocapacitors also generally have weaker cycling stability because redox reactions are less reversible than ion adsorption.

Pseudocapacitive materials have often complemented EDLCs as composites, however, it is also beginning to complement as asymmetric supercapacitors. Supercapacitors that are comprised of one EDLC electrode and one faradaic electrode are known as hybrid supercapacitors. This recent development combines the benefits of ELDCs and faradaic capacitors while mitigating each other weakness. One electrode is composed of a carbon-derivative material that collects capacitance electrostatically, while the other electrode collects capacitance via redox reactions. As a result, improved cell voltage, energy/power densities, and cycling stability (compared to pure faradaic capacitors) can be observed.

## 2.2    Graphene
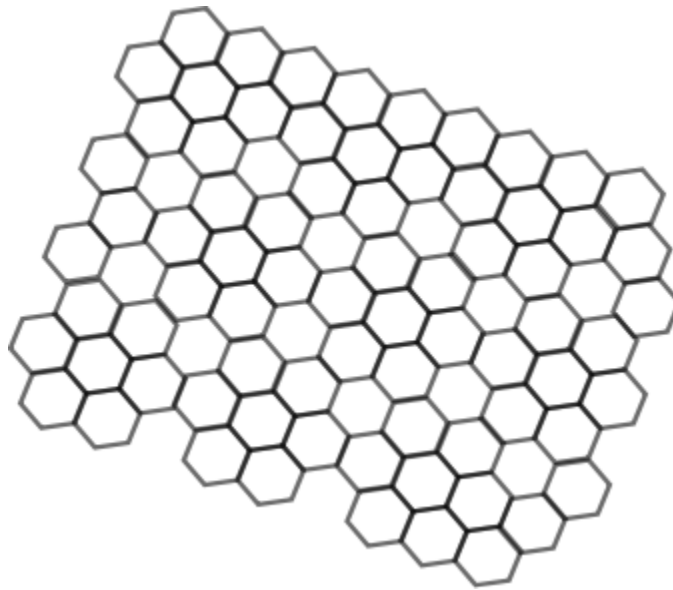


**Figure 6. Honeycomb structure of graphene**

Graphene, one or few two-dimensional sheets of $sp^2$-hybridized honeycomb network of carbon (Figure 6), is a very versatile material beginning to be manifested in many technologies. It is the derivative of many other dimensional allotropes:

- 0-D: Wrapped to form Fullerene

- 0-D: Cutting to form Graphene quantum dots (GQD)[16]

- 1-D: Rolled to form carbon nanotubes (CNT)

- 3-D: Stacked to form graphene nanoplatelets or graphite

Although not a dimensional allotrope, it can be graphene and graphite can be oxidized to form graphene/graphitic oxide.

Although graphene-based materials were discovered in the nineteenth century, research was only recently rekindled in 2004 by Geim and Novoselov from the University of Manchester. They discovered the "scotch-tape method" of obtaining graphene. This method involves the mechanical exfoliation of two-

dimensional graphene from three-dimensional graphite. This discovery led to their receiving of the Nobel Prize in physics in 2010 "*for groundbreaking experiments regarding the two-dimensional material graphene*".[17] Immediately an eruption of interest occurred because two-dimensional crystals were previously thought to be thermodynamically unstable at finite temperatures.[18]

Graphene is a zero-bandgap semiconductor endowed with excellent electrical and thermal conductivity and flexibility, enabling the storage of electric charges, ions and hydrogen.[19] Graphene possesses a very high theoretical surface area ($2630 \text{ m}^2/\text{g}$)[19] as well as high mechanical strength (due to the $sp^2$ bonds). Graphene is near transparent, relative ease to functionalize and has great potential for large-scale production.

Graphene has begun to establish itself in various applications. Within energy, as a strong current collector, graphene is implemented into fuel cells, batteries, solar cells, supercapacitors. Its superior mechanical strength lends itself to mechanically reinforce existing technology (ex. Sports equipment). Lastly, the amazing optical properties and ease of functionalization of graphene manifests itself in applications such as touch screen, light generation, water/air filtration, and among many others.

### 2.2.1 Graphene Synthesis

The eruption of interest in graphene has generated many techniques to prepare graphene. From the top-down approach, there is mechanical and chemical exfoliation,[20] and nanotube slicing. From bottom-up production is the carbon dioxide reduction[21] and epitaxial growth, [22] which also includes chemical vapor deposition (CVD).

#### *2.2.1.1 Oxidation*

The chemical approach was seemingly more practical to upscale rather than via scotch-tape or epitaxial growth. The underlying challenge in producing graphene from graphite is overcoming the strong interlayer Van der Waals forces. Various oxidation methods have been explored, including intercalation, chemical derivatization, thermal expansion, oxidation-reduction and/or use of surfactants.[23] Academically,

graphene synthesis most commonly uses strong oxidizing agents to produce graphene oxide (GO) then chemically reduce GO to produce reduced graphene oxide (rGO).

Chemical oxidation was first reported in literature as Brodie's Method in 1859.[24] Brodie et al. added potassium chlorate ($KClO_3$) to a slurry of graphite and fuming nitric acid.[24] Unfortunately, this generated toxic gases (i.e. $NO_2$, $N_2O_4$, and $ClO_2$) and potassium chlorate is very explosive. Years after, Staudenmaier reinvestigated this matter in 1898.[25] Staudenmaier's method involved the addition of $KClO_3$ to graphite in mixture of concentrated sulfuric acid and concentrated nitric acid. Regrettably, this method was very time consuming as it took over a week for cooling alone. Additionally, it was still dangerous due to $ClO_2$ evolution and the presence of at least 10 g of potassium chlorate, which is a very explosive compound.

Over half a century after Staudenmaier's work, Hummer improved upon both Brodie's and Staudenmaier's method in 1958.[20] Instead, Hummer oxidized graphite with $KMnO_4$ and $NaNO_3$ in concentrated $H_2SO_4$. Hummer's method required less than 2 hours to complete and was safely operable below 45 °C. The active oxidative species was diamanganese heptoxide ($Mn_2O_7$).[20] Very recently, James Tour proposed another method of oxidizing graphite.[23] He proposed the replacement of $NaNO_3$ with phosphoric acid ($H_3PO_4$); small aliquots of $KMnO_4$ in a 9:1 mixture of $H_2SO_4:H_3PO_4$. Marcano et al. claimed that $H_3PO_4$ will ensure more intact graphitic basal planes based on an earlier report of scalable preparation of graphene oxide nanoribbons (GONRs) from multi-walled carbon nanotubes (MWCNT).[23] Additionally, their method overall involves a simpler protocol, higher yield and no toxic gas evolution.

### 2.2.1.2    Graphene oxide (GO)

Graphene oxide, the oxidized derivative of graphene/graphite, is a semi-conductor first reported by Brodie. After the oxidation of graphite, Brodie noticed an increase in the overall mass.[24] In fact, successive oxidative treatments increased oxygen content, however the oxygen content reached a limit

after 4 treatments.[24] Unfortunately, Brodie was mistaken in trying to find a discrete molecular formula for graphite and graphitic oxide.

The actual model of graphene oxide has still remained elusive to scientists, even today. It is however widely accepted that graphene oxide is constituted of graphene sheets with oxygen functional groups on the basal plane and on the edges (ex. epoxides, alcohols, ketone carbonyls and carboxylic groups).[26] These oxygen functional groups disrupt the $sp^2$ bonding networks, bestowing GO its electrically insulating property. These oxygen-containing functional groups also enable GO to be easily dispersed in water, in fact, this advantage is utilized in uniformly depositing GO onto various substrates to form thin films.
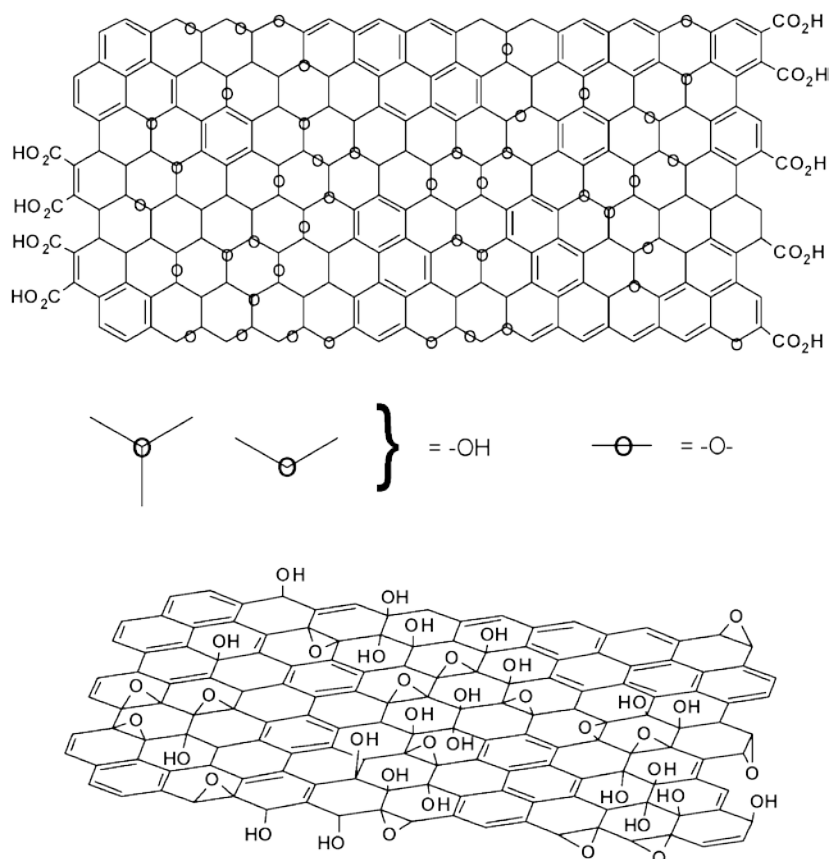


Figure 7. Variations of Lerf-Klinowski model indicating ambuguity of presence of carboxyl groups. Reproduced Adapted from Dreyer et al. [26] with permisssion of The Royal Society of Chemistry.

The exact model of GO has been under debate for recent years and no conclusive model exists.[26] However, Anton Lerf and Jacek Klinowski's model has been widely accepted amongst the graphene community (Figure 7).[26] Lerf et al characterized GO via nuclear magnetic resonance (NMR) spectroscopy.[27]

### 2.2.1.3    Reduction

Reduction of GO involves the restoration of π-network, which thereby restores electrical conductive property. A few common methods of reducing GO include irradiation, thermal and chemical reduction.

Irradiation includes UV Irradiation, by which water when excited, homolyzes into hydrogen atoms, hydroperoxyl radicals and hydrated electrons.[28] These hydrated electrons serve as a very powerful reducing agent.[28] Another form of irradiation is microwave irradiation, whereby oxygen-containing groups are removed via microwave exposure.[29]
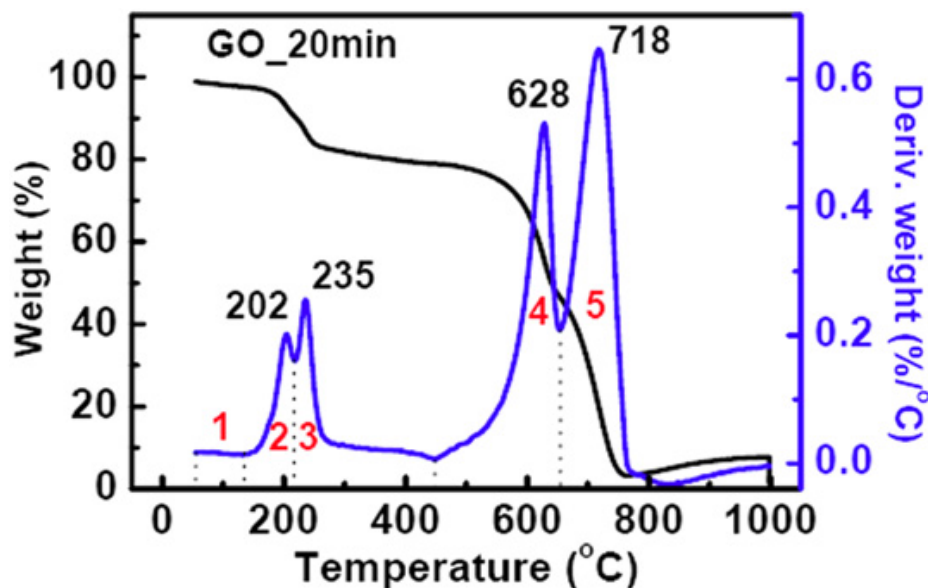


**Figure 8. TGA and DSC profile of GO. Reproduced from Jeong et al.[30] Copyright 2010 IOP Publishing**

Thermal degradation profiles of GO can be generated by characterization techniques i.e. thermogravimetric analysis (TGA) and differential scanning calorimetry (DSC). From Figure 8, under 120 °C, evaporation of water occurs. At about 200 °C and 235 °C, loss in mass can be attributed to hydroxyl and carboxyl groups respectively.[30] 630 - 720 $^o$C were ascribed to the burning and restoration of $sp^2$ carbon backbones.[30]



**Figure 9. Photographic comparison of GO foam undergoing a slow and rapid thermal reduction**

A rapid thermal reduction will induces rapid degassing, often inducing large cracks in the basal plane and sometimes macro-structural collapse (Figure 9). A special case of rapid thermal reduction is called flash heating, by which GO undergo flash heating to a very high temperature, followed by flash quenching, whereby the GO is exposed to room temperature shortly after.

Lastly, albeit chemical reduction is the most commonly used reduction technique, unfortunately, the graphitic basal plane is not fully restored and significant defects are left on the $sp^2$ plane. As a result, chemically reduced GO is often referred to as reduced graphene oxide (rGO). The most common and pioneering GO-reducing chemical is hydrazine monohydrate.[31] Unfortunately, hydrazine is highly toxic and unstable in its anhydrous form, thus other reducing agents (ex. ascorbic acid) were investigated and discovered.[32] Depending on the reducing agent, heteroatomic impurities can also be introduced onto rGO

(ex. Nitrogen groups via urea).[33] Unfortunately, no simple route exists for removing these impurities.[31] Alternative reducing agents that have been reported in literature include sodium borohydride (NaBH$_4$),[34] hydroquinone,[35] and other strong alkaline solutions.[36]

### 2.2.2 Technical Challenges

Despite the research advances made in graphene, rGO is often setback due to the tendency to agglomerate upon reduction. When applied to supercapacitors, agglomeration will decrease the effective surface area for electrostatic charge accumulation. Additionally, this phenomenon can hinder ion diffusion.[37]

Common agglomeration-mitigation practices include manipulating the graphene architecture, so also to increase the surface area. Graphene has be molded into films, foams, fibers, via CVD,[38] templating,[39] casting,[38] and hydrothermal techniques.[39] With the proper reduction precursors, certain functional groups can also act as spacers between graphene sheets to prevent complete agglomeration. The functional groups can operate via electrostatic repulsive forces or from their inherent, bulky size.[40] Another example is preparing short carbon chains with graphene-surface reactive groups on each end, which can be obtained via the precursor, ethylenediamine (EDA).[40]

Currently, the primary deterrent to mass manufacturing and widespread use of graphene is the lack of a reliable, economical method that can produce high quality samples in a scalable production.[41] However, recent research has reported to grow graphene on existing industrial Cold-wall CVD.[42] NanoCVD, a cold-wall CVD, is currently used in the semiconductor industry. Bointon et al. has reported to be able to mass produce graphene with enhanced electronic quality.[42] This technique was announced to be 100 times faster and 99% lower in cost than standard CVD.[42] Another research group has mentioned that melting a thin film of silica onto platinum to fill platinum's topographic defects, promotes epitaxial graphene growth when passing methane gas atop.[43] Babenko et al. has described that 15 minutes of this CVD configuration has produced large graphene crystals around 2-3mm. In comparison, it usually takes up to 19 hours with current CVD techniques to generate a crystal of that size. There were also fewer grain boundaries (edge defects), which improves thermal/electrical conductivity.[43] At the current rate of

graphene technology development, increased incorporation of graphene will be inevitable realized in the

near future.

# 3.0  Characterization

## 3.1  Structural Characterizations

### 3.1.1  Scanning Electron Microscopy (SEM)

Scanning Electron Microscopy (SEM) is perhaps the most popular and versatile method to view topological features and atomic compositions and even electrical conductivities. SEM is capable of viewing both organic and inorganic materials enabling widespread usage across many fields (materials science, forensics, biological samples). The only caveat is that scanned surface of the sample must be electronically conductive. Fortunately, sputtering conductive nanoparticles (ex. Carbon or gold) is a popular to fulfill this requirement albeit these particles can be seen at very high magnifications. SEM is capable in producing three-dimensional like images of surfaces due to its large depth of field. The magnification spans from micrometres (μm) to nanometers (nm).
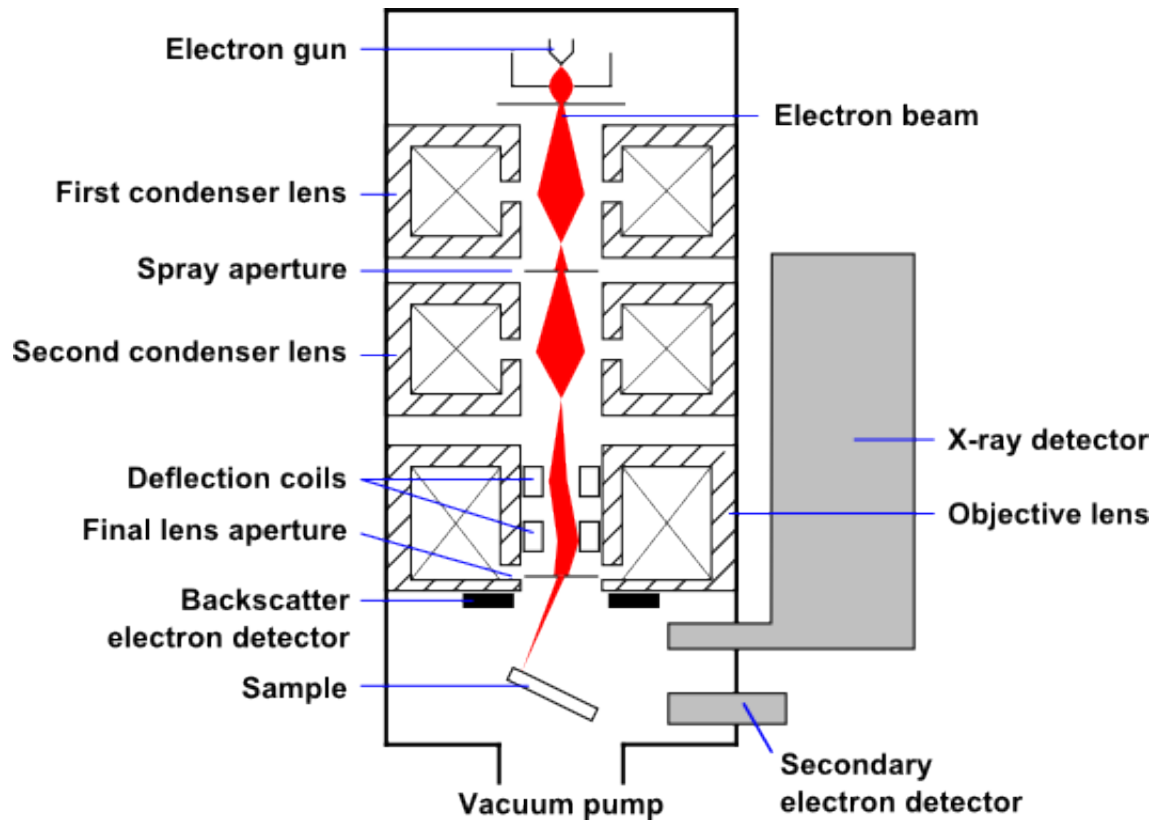
**Figure 10. Diagram of SEM tracing the main components. This work is attributed to Steff.**

The operational components of an SEM are displayed in Figure 10. The operation of SEM begins with the beam gun generating finely focused beam of high energy electrons that is swept across the surface of specimen.[44] The electrons decelerate after hitting sample and generate a variety of signals. These signals are reflected in the form of secondary electrons, which can be translated to the morphology and topography; backscattered electrons which can be used to illustrate the contrasts in composition; diffracted backscattered electrons; phonons, which are used for elemental analysis and continuum x-rays; as well as visible light and heat.[44] These signals are collected by specifically located detectors (Figure 10).[44]

The diameter of the generated electron beam limits the image resolution.[44] The electron current flowing through the final probe determines the intensity of the secondary and backscattered electron and x-ray signals.[44] Lastly, the angle of the conical beam determines the height of depth of field. In this work, SEM will be used to confirm the morphology of the graphene foam structure. Additionally, it will serve to confirm the uniform and thorough wrapping of GO and rGO onto the surface of the nickel mesh.

### 3.1.2  Transmission Electron Microscopy (TEM)

Another popular imaging characterization technique is the Transmission Electron Microscopy (TEM). TEM is a microscopy technique that is capable of significantly higher resolution than light-based microscopy due to the de Broglie wavelengths. This enables fine detailed images, even down to the atomic level. Similar to SEM, its application is vast and can be found in various fields such as microbiology, nanotechnology, in-situ reactions, pollution mitigation, etc.
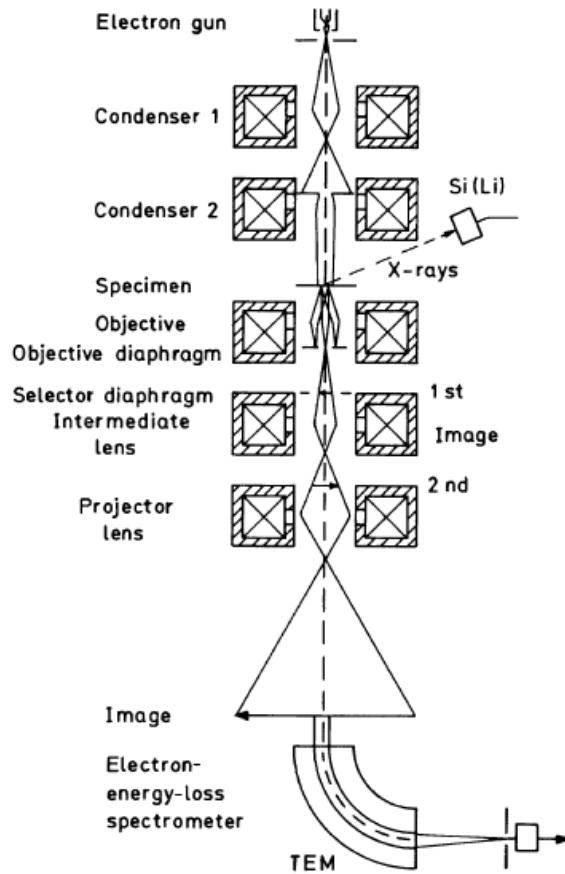
**Figure 11. Schematic of path of ray within a TEM equipped additionally with x-ray and electron energy-loss spectroscopy**[45]

Figure 11 presents the schematic pathway for how the generated ray would traverse within a TEM. Firstly, electrons are emitted from an electron source via either thermionic, Schottky or field emission. Field emission is needed to generate higher electron intensities and coherence.[45] A three or four-stage condenser-lens system controls the aperture of illumination, which results in controlling the illumination area of the sample. The distribution of the electron intensity is then captured by a lens system onto a fluorescent screen. The distribution is then translated into an image via photographic emulsion or by coupling the fluorescent screen to a fiber-optic plate that's connected to a CCD camera.[45]

20

The atoms after subjection to the electrons undergo elastic and inelastic scattering.[45] Therefore, the specimen must be very thin (less than 100 nm). The power requirement for the electron source depends on the density and elemental composition of the object, and especially the resolution desired. To reduce excess background noise, samples should be mounted on to a thin metal grid (i.e. copper).[44]

In this thesis, due to the strict sample thickness requirement, TEM will be utilized to view the lateral sheet size of GO.

### 3.1.3   X-Ray Diffraction (XRD)

X-ray diffraction (XRD) is a popular structural characterization technique that is often used to study crystal structures. Sample diffraction is the scattering of radiation on a regular array of scattering centers, whereby in this case, would be the atoms of the sample.

The XRD is comprised of 3 basic elements:

1. X-ray tube (cathode ray tube)
2. Sample holder
3. X-ray detector

In XRD, either the X-ray tube and detector rotate simultaneously, or only the X-ray tube rotates, and detector remains stationary. X-rays are generated in the x-ray tube, filtered for monochromatic radiation, then collimated and directed at sample.[46]
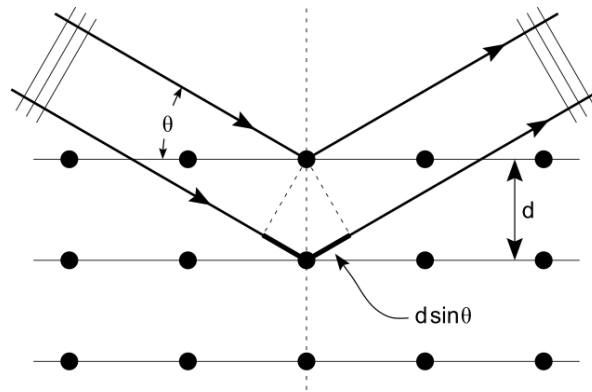
Figure 12 depicts the operation of x-ray diffraction within a sample. The crystal sample acts as a three-dimensional diffraction grating, which causes light to be scattered in specific directions. The scattering is due to the interaction between the photon of an electromagnetic radiation and an orbital electron from an atom. The precise direction is a function of the exact spacing between the repeated stacking of the crystal planes.

Bragg's law describes the condition for diffraction. The X-ray beams scattered off an adjacent in-phase crystal plane will result in constructive interference. If the crystal is out-of-phase, the scattering will result in destructive interference and no scattering intensity will be detected. This phenomena is summarized in Bragg's law (Equation 1), which relates the wavelength of the electromagnetic radiation to diffraction angle and lattice spacing:[46]

$$n\lambda = 2d \ sin\theta \tag{1}$$

Where n is an integer, $\lambda$ is the wavelength of the x-ray, d is the interplanar spacing detected from the diffraction signal, and $\theta$ is the diffraction angle. In the case of graphene at the (002) plane, the lattice spacing will correspond to the inter-sheet distance.

Additionally, the crystallite size can be estimated using the Scherrer Equation:[47]

$$L_C = \frac{A\lambda}{B\cos\theta} \tag{2}$$

Where A is the shape factor (~0.9), $\lambda$ is the x-ray wavelength, B is the full width at half maximum (FWHM) of the (002) peak in radians. In turn, the crystallite size can be estimated via:

$$\# \ of \ layers = \frac{L_c}{d-spacing} \tag{3}$$

In this work, XRD will be used to confirm the successful synthesis of GO and rGO based on comparisons to literature.

### 3.1.4 Braunauer-Emmett-Teller (BET) Specific Surface Area Analysis

Braunauer-Emmett-Teller (BET) is not actually a characterization technique, but rather, a widely used theory used to analyze surface area and pore distribution data. It serves as a basis to correlate the physical adsorption of gas molecules onto a surface, and the material's effective surface area. This theory is built upon the foundational Langmuir theory which was initially established for monolayer adsorption.

BET is applicable for multilayer adsorption using the following three assumptions:[48]

  I.   Gas molecules molecule can physically adsorb onto solid with infinite layers

  II.  No interaction between each adsorption layer

  III. Langmuir theory can be applied to each layer

The resulting equation is as follows:[48]

$$\frac{1}{\left[V_a\left(\frac{P_0}{P}-1\right)\right]} = \frac{C-1}{V_m C} * \frac{P}{P_0} + \frac{1}{V_m C} \tag{4}$$

Where P is partial vapour pressure of adsorbate gas in equilibrium with surface [Pa], $P_0$ is the saturated pressure of adsorbate gas [Pa], $V_a$ represents the volume of gas adsorbed at standard temperature and pressure [mm], $V_m$ is the volume of gas adsorbed at STP to produce apparent monolayer at sample surface [mm], and C is the BET constant.

Surface area analysis begins by degassing the chamber to remove residual gases and vapours. Sufficient volume of adsorbate gas (an inert gas, ex. Ar, $N_2$) is admitted into chamber until the lowest desired relative pressure is attained. $V_a$ is measured at successively higher $P/P_0$ values enabling a continuous plot of Equation 4, by which the $V_m$ and the BET constant C can be calculated. Once these values are obtained, the specific surface area can be derived from the cross-sectional area of the adsorbate and the mass of the sample.

Surface area quantification is particularly important to characterizing supercapacitor electrodes because specific surface area will correlate directly to the effective area available for electrostatic accumulation. However, the variation in this work via BET was found to be quite large, instead, UV-Vis Spectroscopy utilizing methylene blue adsorption will be used.

### 3.1.5 Ultraviolet-Visible Spectroscopy (UV-Vis)

Ultraviolet-visible spectroscopy (UV-Vis) involves quantifying the attenuation of the beam of light after reflecting/passing through the sample. This adsorption/reflectance spectroscopy measures the wavelength from the ultraviolet to visible spectrum (190-1100 nm). UV-Vis is used in many applications that require detection of functional groups, impurities. UV-Vis has been used for both qualitative and quantitative analysis.
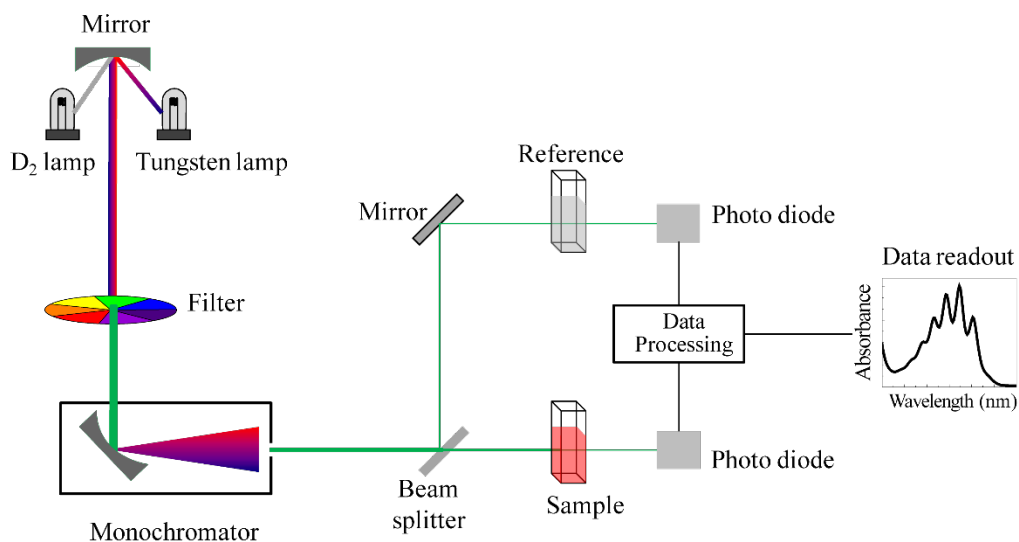
**Figure 13. Schematic of the operation within a UV-Vis Spectrometer. This work is attributed to Sobarwiki.**

Figure 13 exhibits the operation of a typical UV-Vis. The UV-Vis is basically comprised of a radiant source, a series of wavelength filters, a cuvette containing the solvent (and sample) and lastly a photo-detector to display the results. The light source emits beam of light is filtered through a diffraction grating, and then focused by a slit. The laser subsequently passes through the solvent-submerged sample and then directed into the detector. The detector converts the incoming light into current and compares the intensity of the light passing though the reference and the sample. This current can be translated to absorbance via Equation 5:[49]

$$A = log_{10} \frac{I_0}{I} \tag{5}$$

Where $I_0$ and $I$, is the current translated from the light that passed through the reference and the sample respectively. For practical usage, beer Lambert's Law relates absorbance 'A' to concentration '$c$':[49]

$$A = \varepsilon cL \tag{6}$$

Where $\varepsilon$ is the molar extinction coefficient of compound, and L is the path length.

UV-Vis is especially useful for analyzing molecules that pi-electrons and non-bonding n-electrons. These electrons imparted with energy, can be excited from the highest occupied molecular orbital (HOMO) to the lowest unoccupied molecular orbital (LUMO). [49]

In this thesis, UV-Vis will be used to measure the concentration of methylene blue before and after exposed to reduced graphene oxide deposited on nickel foam electrodes. This difference in concentration will allow qualitative assessment of the surface area available for electrostatic accumulation.

### 3.1.5.1 Methylene Blue Surface Area Analysis

Methylene Blue (MB) is organic dye that readily dissolves in water.
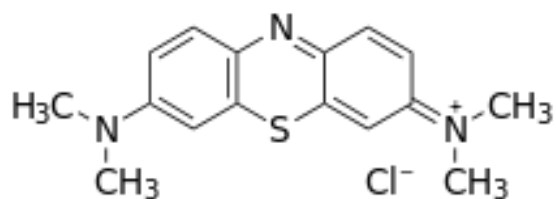


Figure 14. Skeletal structural formula of Methylene Blue

As shown from the skeletal structural formula (Figure 14), MB's molecular formula is $C_{16}H_{18}N_3SCl$ and has a MW of 319.85. It is commonly applied in dyeing cotton, wool, coloring, hair, etc. It has a strong adsorption onto solids, which makes it a model antagonist when evaluating dye and organic contaminant removal from aqueous solutions.[50]

MB has demonstrated in literature to be an effective adsorbate for qualitatively measuring surface area of graphene-based products.[51] Firstly, a calibration curve is setup by measuring known concentrations of aqueous MB in the UV-Vis spectroscopy. Then the concentration of the MB solution before and after mixing in graphene sample is measure. There is an assumption that must be made: MB will only

monolayer adsorb onto graphite/graphene. With this assumption the amount of MB adsorbed can be derived via Equation 7:

$$q_e = \left(\frac{C_0 - C_e}{m}\right) V \tag{7}$$

Where $C_0$ and $C_e$ are initial and equilibrium concentration of MB in solution [mg/L], V is the volume of solution [L], and m is mass of adsorbent [g]. After calculating the amount of MB adsorbed, literature has related 2.54 $m^2$ of surface covered per mg of MB adsorbed[51]

In this work, MB and UV-Vis was used to qualitatively determine the specific surface area available for electrostatic accumulation on the reduced graphene oxide-nickel electrodes.

### 3.1.6   Raman Spectroscopy

Raman Spectroscopy is a fast, non-destructive, capable of high resolution, structural and electronic information, and reproducible technique.[52] It is a popular characterization technique for carbon-based samples, such as: amorphous carbons, fullerenes, nanotubes, diamonds, carbon chains, etc.
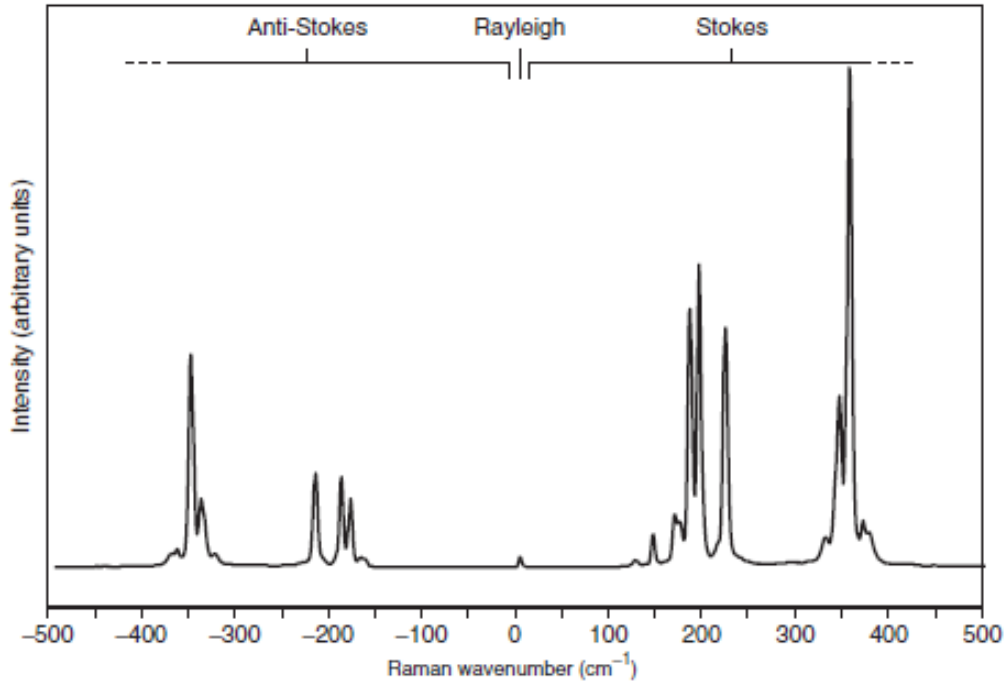
**Figure 15. Raman spectrum example demonstrating anti-Stokes region, Rayleigh line, and Stokes region[53]**

Within the Raman spectrometer, an intense, monochromatic beam of electromagnetic radiation is focused at sample, inducing a dipole moment.[53] This induced dipole moment involves 3 components, as seen in Figure 15:

I.  Elastic scattering of electromagnetic radiation (also known as Rayleigh scattering)

    In this scenario, the system returns to its initial state, that is, the frequency of the emitted photon is at same frequency of incident photon.

II. Inelastic scattering of electromagnetic radiation (also known as Raman scattering)

    This can be further subdivided into 2 categories:

    a.  Anti-stokes scattering, which occurs when there is higher energy of scattered radiation compared to incident beam. This results in a downshift in frequency

    b.  Stokes scattering, which occurs when there is lower energy of scattered radiation compared to incident beam. This results in a upshift in frequency

28

The size of the dipole moment is dependent on charge separation. Larger internuclear distance means electrons are farther away from nuclei and can move more easily. Vibrational movement of the molecule include symmetrical stretch vibration, asymmetrical stretch and bending vibrations. Raman and infrared activity depends on the orientation of these molecules.

Both, the atomic structure and electronic properties of graphene can be extracted from Raman spectroscopy due to absence of band gap making all wavelengths of incident radiation resonant.[51] Raman spectroscopy can be used to identify defects, structural damage, functional groups and chemical modifications.[51]
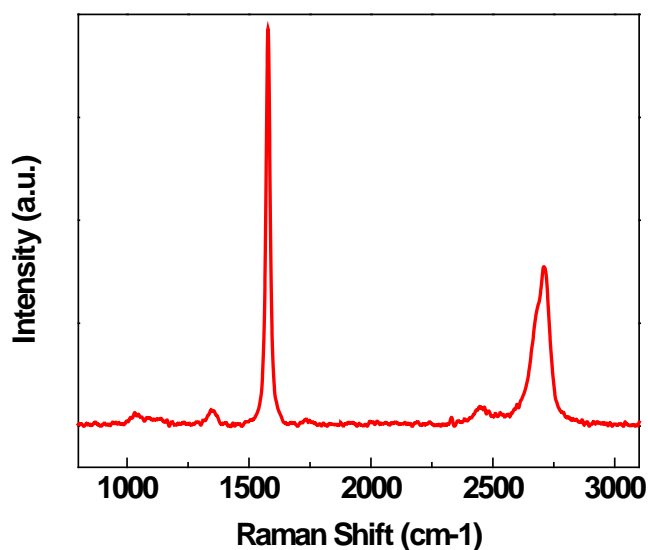


**Figure 16. Raman Spectra of powder graphite**

As seen in Figure 16 for graphene-based products, the Raman spectra often display 3 distinct peaks, which correspond to the D, G, and 2D peak. The D peak (Disorder) is detected only in a small region of the crystal near a defect or an edge.[52] The intensity of the D peak ($I_D$) is proportional to number of defects at probed location.[52] This peak can typically be located at ~1350cm$^{-1}$. The G peak (Graphite) corresponds to the first order scattering of stretching vibration mode observed on sp$^2$ carbon domains. The intensity of

the G peak ($I_G$) is related to relative motion of $sp^2$ carbons and is independent from disorder.[52] This peak can be typically found at ~1580cm$^{-1}$. The 2D peak is actually an overtone of the G peak (~1580cm$^{-1}$) can be typically found at ~2700cm$^{-1}$. The $I_D/I_G$ ratio is a ratio commonly used to quantify the average size of $sp^2$ domains or to measure disorder within graphene. Tuinstra and Koenig derived a relationship (Equation 8) that can be used to relate the $I_D/I_G$ ratio to the interdefect distance:[54]

$$L_a[nm] = (2.4 * 10^{-10})\lambda(^{I_D}/_{I_G})^{-1} \tag{8}$$

Where $\lambda$ is the Raman excitation wavelength of the laser.

Raman spectroscopy will be used to confirming the presence of graphene and help elucidate the reason for the capacitance and resistance data.

## 3.2    Electrochemical Characterizations

Electrochemistry is the study of chemical response to electrical stimulation. It is use to understand the loss or gain of electrons (oxidation/reduction) under electrical stimulation. These redox reactions provide information concentration, kinetics, reaction mechanisms and chemical systems.

In an electrochemical experiment, one of the four following parameters is measured or controlled:[55]

- Potential
- Current
- Charge
- Time

Electrochemical characterizations are use ubiquitously, from neurotransmitter behaviour to initiator behavior in polymerization to battery kinetics.[56]

### 3.2.1 Half-Cell Design

A half-cell mimics the environment of one electrode in a full-cell system. The behavior of a single electrode and its reactions are independent of whether the electrode was involved in an electrolytic or galvanic cell. Half-cell designs are generally used for preliminary screening due to the small amount of material that is required to obtain electrochemical data.
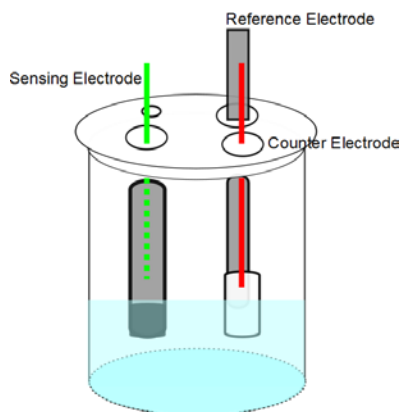


**Figure 17. Typical Half-cell setup**

As presented in Figure 17, a half cell is typically comprised of a conductive electrode (typically glassy carbon), a counter electrode (typically platinum), a reference electrode and the electrolyte for the ions to diffuse through. The conductive electrode within the electrolyte will be encased in a naturally occurring double layer, by which reactions can occur. However, due to the impractical application of half-cells, electrodes are often incorporated into full cells to mimic commercial situations.

rGO formulations were originally screened via depositing 40 ng onto the surface of a glassy carbon, followed by electrochemical characterizations described in the following sections. However, rGO were impregnated into nickel-foam to prepare full-cells for a more practical evaluation.

### 3.2.2 Cyclic Voltammetry (CV)

Cyclic Voltammetry (CV) is one of the more commonly used electroanalytical techniques. CV is primarily used to characterize a system. A single CV scan is not very suitable for quantitative evaluation, as it can only hint to the phenomena occurring in the electrochemical system. However, multiple CV can be used for many applications, such as: determination of reversible/irreversible behaviour of redox couple, number of electrons transferred in redox reaction, formal potentials, rate constants, formation constants, reaction mechanisms, diffusion coefficients.[55] Multiple CVs also mimics environments that are closer to the steady-state or allow buildup of reaction products at the electrode surface.
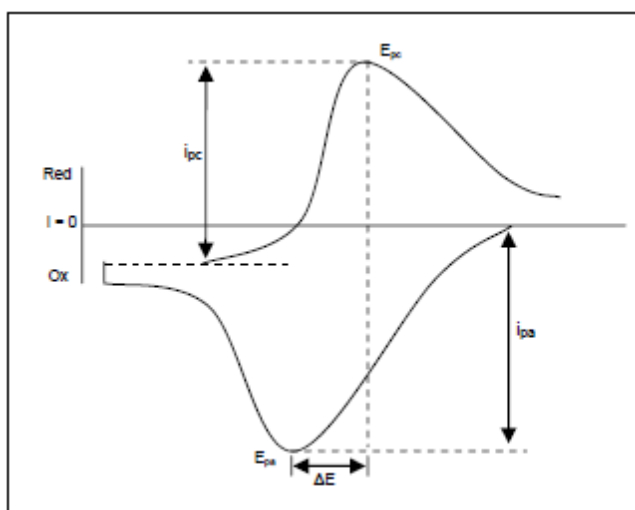


**Figure 18. Typical Cyclic Voltammagram of a reversible electrochemical reaction.[55]**

In CV, the potential gradually changes via the application of a potential ramp to the working electrode, then reverses the scan to the initial potential. The current is simultaneously measured as a response to the potential sweep. The current and potential values are extracted and used to plot the CV curve.
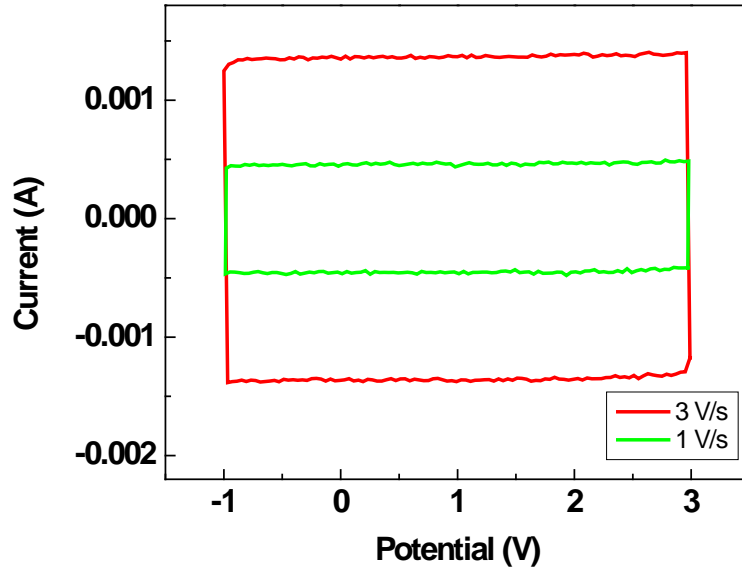
**Figure 19. CV of 40 µF Commercial Capacitor at two different scan rates**

Figure 19 depicts the CV of a typical commercial capacitor (or ideal supercapacitor behavior). The rectangular shape regardless of scan rate highlights the rapid electrostatic accumulation, i.e. low resistance throughout the cell.

Half-cell capacitance can be calculated via:[57]

$$C_S = \frac{\int i \, dV}{2 * m * \Delta V * s} \tag{9}$$

Where $\int i dV$ is the integration of the area under the curve, $m$ is the mass, $\Delta V$ is the voltage range that the CV was scanned to and $s$ is the scan rate of the voltage sweep. The full cell capacitance can be calculated via Equation 10:[57]

$$C_{S,Full-cell} = C_{S,Half-cell} * 4 \tag{10}$$

CV will be utilized primarily to quantify and calculate the capacitance of the as-prepared coin-cell supercapacitors. In this work, multiple CVs were made at each scan rate, however, only the last CV of each scan rate will be recorded. This was conducted to remove any "activation" effects from charging and discharging new supercapacitors.

### 3.2.3 Galvanostatic Charge/Discharge (GCD)

Galvanostatic Charge/Discharge (GCD) is also known as chronopotentiometry. It can be used to detect presence of redox reaction in energy storage systems, similar to CV.[55] It is often seen used in corrosion analysis, battery charge/discharge cycling.

As the name implies, chronopotentiometry applies a constant or step current to measure potential as a function of time.

The capacitance can be calculated via equation 11:[57]

$$C = \frac{I}{dV/dt} \tag{11}$$

Where I is the discharge current and dV/dt is the change of potential over a set duration.

One variant usage of the GCD plot is to repeat charge and discharge for 1000s of cycles. This will simulate the cycling stability over a large amount of usage. One of the major strengths of Supercapacitors is its long cycling stability. This is due to the energy storage method, ion adsorption on the surface of the electrode (Figure 4), does not undertake major chemical or physical changes (ex. Silicon fracturing from repeated lithium intercalation)[58].
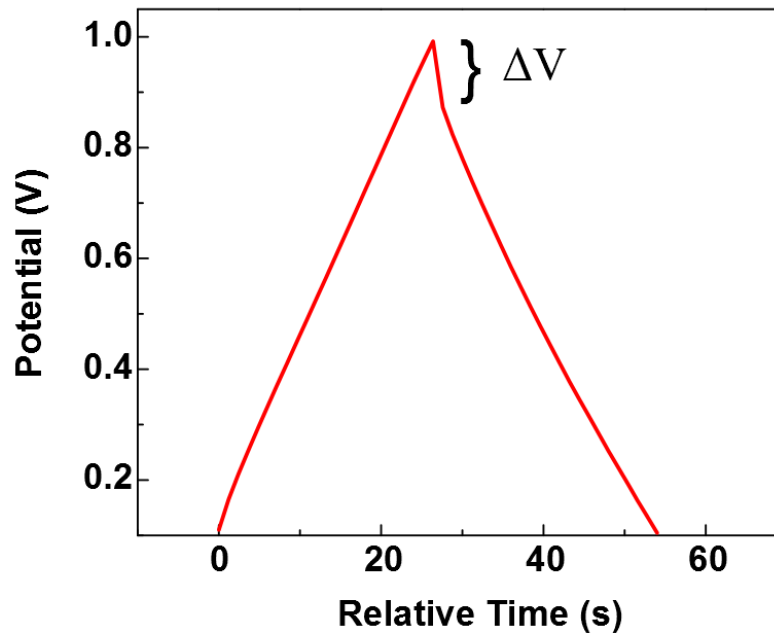
**Figure 20. Single GCD graphene of a typical supercapacitor highlighting the ohmic drop**

The equivalent series resistance (ESR) can also be calculated from the ohmic drop (vertical line as depicted by ΔV in Figure 20) observed at each initial discharge in a GCD graph as shown in equation 12:[7]

$$ESR = \frac{\Delta V}{\Delta I} \tag{12}$$

Where ΔV is the voltage drop, and ΔI is the corresponding discharging current.

GCD will be used to verify the capacitance obtained from CV and for comparing the calculated ESR amongst the samples.

### 3.2.4 Electrochemical Impedance Spectroscopy (EIS)

Electrochemical Impedance Spectroscopy (EIS) is used to measure the ionic/electrical resistance of a sample. Equation 13 depicts the scenario of an ideal resistor (Ohm's Law):

$$R = V/I \tag{13}$$

Where R is the real resistance, V is the voltage and I is the current.
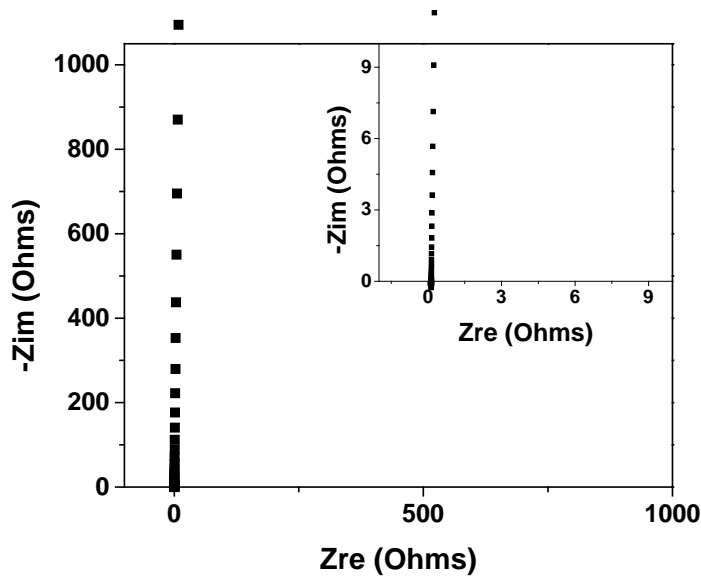


**Figure 21. EIS plot of commercial 40 μF capacitor**

From Figure 21, the EIS plot of a commercial capacitor (or ideal situation for a supercapacitor) is shown. On a nyquist plot, impedance is depicted on the imaginary axis (-Zim) that's greater than zero. Real resistance is represented on the x-axis (Zre). Figure 21 further confirms the interpretation of the CV (Figure 19) that the capacitor has negligible real resistance.

However, real-life situation are usually far more complex. Thus in the case of EIS, a small excitation signal is used to induce a pseudo-linear response, of which can be modelled/fitted onto an equivalent circuit.[59]
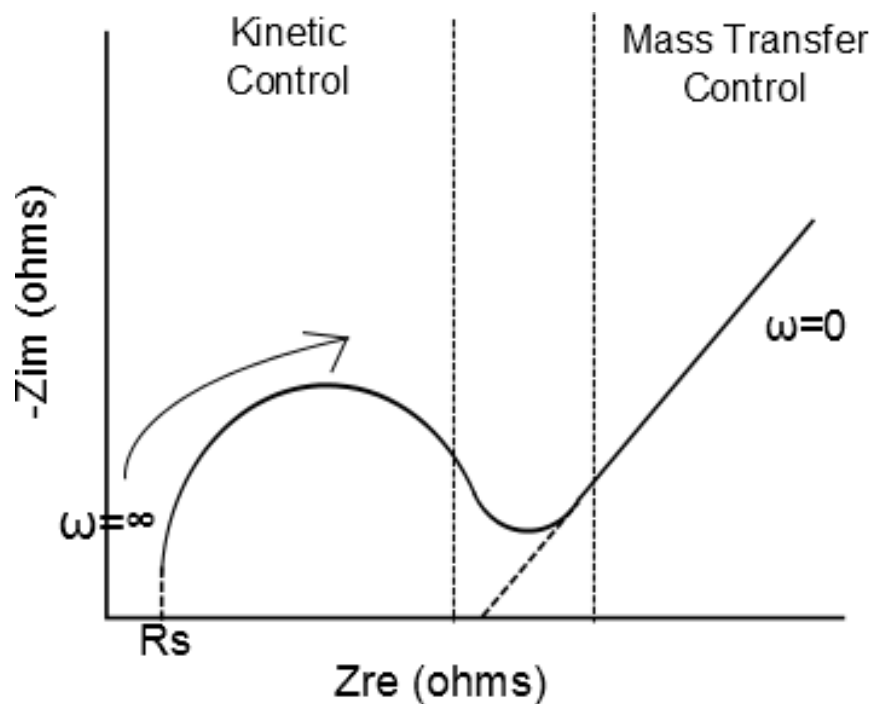
Figure 22. Typical Nyquist plot of EDLCs

An AC potential is applied to the electrochemical cell and the current is measured. The obtained data is often displayed in the form of nyquist plots (Figure 22) and bode plots. Nyquist plots are graphs of the imaginary resistance (impedance) as a function of the real resistance.

As introduced in Figure 22, the $R_S$ is the x-intercept on the nyquist plot. This is the sum of the inherent resistance of each component within cell excluding any interactions between components (ex. Current collector, electrode, electrolyte, etc.).[7] The semi-circle represents the charge transfer resistance.[7] The mass transfer region is typically modelled with the "infinite" Warburg impedance, and this represents capacitive charging.[11] This depicts the physical phenomenon of the diffusion of ions from the bulk liquid to the surface of electrode for electrostatic accumulation. The region between the kinetic to mass transfer control regions is the transition between frequency dependent diffusion to capacitive charging.[7]

This thesis will involve the thorough investigation and interpretation of Nyquist plots to reveal the resistance contribution from different planar sizes of graphene within supercapacitors.

# 4.0　Experimental and Characterization

| Notation | Description |
|---|---|
| s-graphite & L-graphite | Small graphite [2-15 µm] & large graphite [-10 mesh (<1.70mm)] |
| s-GO & L-GO | GO synthesized from small graphite & large graphite (unspecified concentration) |
| s-rGO-3 & L- rGO -3 | Reduced Graphene Oxide obtained from 3mg/mL GO: from small graphite & large graphite |
| s-GO/N-10 & s- rGO/N-10 | Nickel foam dip coated with 9mg/mL of GO (from small graphite) & reduced |
| L-GO/N-20 & L- rGO/N-20 | Nickel foam dip coated with 20mg/mL of GO (from large graphite) & reduced |

To condense the descriptions to differentiate graphite, GO, and rGO prepared at different concentrations of GO, a nomenclature such as that of Table 1 will be used.

Graphene samples derived from graphite power (2-15 µm) will be denoted with a prefix "s-", while graphene samples derived from graphite flake (-10 mesh) will be denoted with the prefix "L-". Coin cell electrodes were prepared by dip-coating nickel foam into GO solutions of varying concentrations: 3 mg/mL, 9 mg/mL, 20 mg/mL and 30 mg/mL. These samples will be denoted with the suffix: "-3", "-9", "-20", and "-30" respectively. Nickel foam dipped in GO will be denoted by GO/N and post-reduction will be denoted by rGO/N.

## 4.1 Graphene Oxide synthesis

Initially both L-Graphite (10 mesh, Alfa Aesar) and s-Graphite (2-15 µm, Alfa Aesar) were subjected to modified Hummer's method.[20] While maintaining rigorous agitation, graphite (1 g) and sodium nitrate (NaNO3, 0.5 g) were mixed in concentrated sulfuric acid (H2SO4, 75 mL). Upon the slow addition of potassium permanganate (KMnO4, 4 g), the solution gradually changed color from black to dark green. The mixture was then left to stir for an additional 3hrs at room temperature. Subsequently, water was added (75 mL), resulting in violent effervescence of the mixture, then left to stir for another 30 min. Additional water (140 mL) was added followed by the slow addition of hydrogen peroxide (H2O2, 20 mL), changing the color of the solution from brown to yellow. The mixture was washed and filtered in hydrochloric acid (HCl, 250 mL, 5 wt%) followed by repeated rinsing with water via centrifugation to remove any residual acid.

s-GO was prepared successfully, however for L-GO, the mixture thickened substantially after addition of $KMnO_4$. A sludge-like mixture developed inducing heterogeneous mixing. Graphite intercalation compound was formed after the graphite was oxidized in $H_2SO_4$ and $NaNO_3$.[60] Afterwards, there were partial unzipping of GO sheets and growth of epoxy groups upon addition of $KMnO_4$.[61] However, this unzipping must have triggered the overdevelopment of graphitic oxide with planar sheets large enough to induce a viscous network. The solution was left mixing overnight, conceiving the possibility that the graphitic oxide would continue to exfoliate until graphene oxide sheets were small enough to lower the viscosity. Unfortunately, the sludge-like mixture remained viscous the following day.

To mitigate the formation of the sludge-like mixture, a pre-treatment was introduced to L-GO to decrease the number of stacked layers prior to oxidation via modified Hummer's method. We adopted the method of preparing expanded graphite previously reported by Yu et al.[62] L-graphite was left soaking in an acid mixture consisting of 3:1 $H_2SO_4$:$HNO_3$ at room temperature overnight. The graphite-acid mixture was then filtered and washed with DI water until pH of filtrate was ~6, then left to dry overnight. Post-drying, the graphite intercalation compound was flash heated to 800 $^{\circ}$C for two minutes followed by flash

quenching at room temperature. This induced a rapid evaporation of intercalated acid within the graphite, forming worm-like "expanded graphite"[62] Applying modified Hummer's method to expanded graphite yielded L-GO.

## 4.2 Supercapacitor Electrode Preparation

The electrodes were prepared via dip-coating nickel foam into various concentrations of GO solution, followed by a mild chemical reduction. 10 mL GO solutions with various concentrations (3, 5, 10, 20, 30 mg/mL) were used.
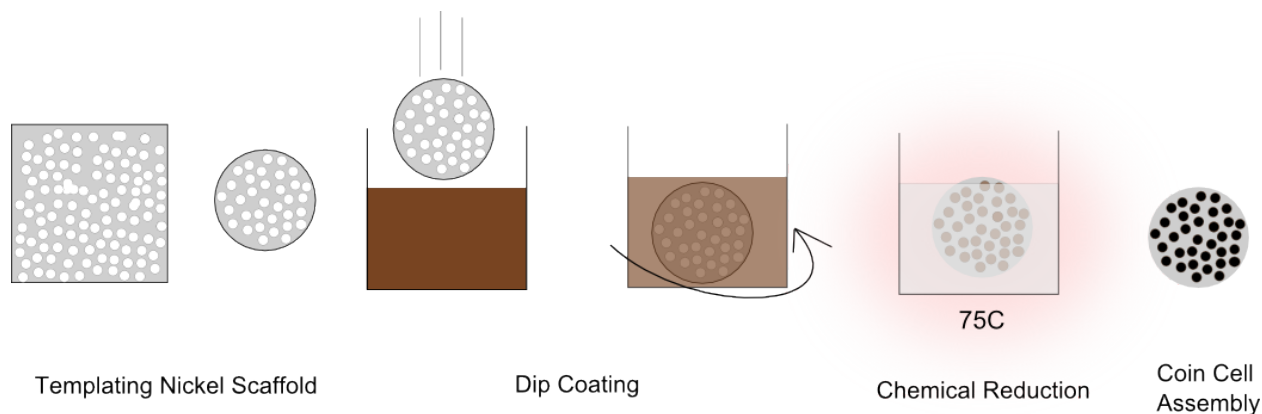
**Figure 23. Schematic of Supercapacitor electrode preparation**

Figure 23 highlights the major phases of the process of preparing the supercapacitor electrodes. Nickel foam (d = 0.70cm) was initially sonicated in acetone for more than two hours to remove impurities on the surface. After drying, porous nickel was immersed in an aqueous GO solution, followed by sonication and vortexing to ensure thorough GO penetration into the nickel framework. Next, the GO/N was immersed into Ethylenediamine (EDA, 10mL, 0.05M) for 4 hours at 75°C, for partial reduction and simultaneous stitching[40]. Each sample was subsequently rinsed with DDI water for 1 hour, and then further reduced in ascorbic acid (10mL, 0.05M) overnight at 75°C, resulting in G/N. The G/N electrodes

were rinsed with water to remove any residual acids, followed by 1000 psi pressing for half a minute, and then freeze-drying overnight to remove any residual water.

The mass of the rGO/N was measured to be less than nickel foam prior to GO dip-coating. Instead, the mass was calculated by comparing the mass before and after removal of rGO via sonicating in ethanol for 48hrs. 25% of the prepared electrodes were degenerated to ensure a statistically reasonable mass loading. Each electrode was soaked in 2M KOH overnight prior to symmetric coin cell assembly for electrochemical testing.

Many efforts were made to investigate and optimize operation parameters. In every case (chronological order), at least 4 electrodes (produces 2 coin cells) were prepared for each investigation.

1. Ethylenediamine (EDA) was introduced as a preliminary reducing agent. EDA acts as a spacer and stitching between graphene sheets preventing agglomeration and simultaneous reduction[40]. As a result, a 40% capacitance increase was found in the presence of EDA. Thus, EDA reduction was locked into the formulation as a reduction step prior to AA reduction.

2. Durations of exposure to Ascorbic Acid (AA) reduction at 70 °C were varied. Hydrothermal and chemical reduction are effective methods of reducing GO to rGO.[63] GO/N electrodes were exposed to AA at 70 °C for 4, 18 and 24 hours and evaluated based on capacitance characterizations. Increasing reduction time from 4 to 18 hours resulted in a 200% capacitance. However, further increasing the reduction effected negligible capacitance improvement. It was postulated that initially, there was insufficient electron conductivity due to the insufficient reduction of GO. Hence, AA reduction was locked to at least 18 hours.

3. At this point, rGO with different planar sizes were considered. rGO prepared from different grain size graphite (2-15 µm and 800 µm) were investigated.  Briefly, s-rGO/N exhibited marginally yet consistently greater capacitance retention than L-rGO/N. However, L-rGO/N displayed marginally lower resistance. Details will be expounded in section 5.0 of this thesis.

4.  $MnO_2$ groups were investigated to increase capacitance via pseudocapacitance. After EDA/AA reduction, rGO/N was exposed to 18 hours of 0.1M $KMnO_4$ The presence of $MnO_2$ depreciated the gravimetric capacitance by 95% from without $MnO_2$ doping. This is most likely due to the significant increase in the mass while the capacitance remained stagnant. As a consequence, $MnO_2$ doping was not considered herein.

5.  Conventional hydrazine reduction was investigated to serve as a potential control.[64] The 0.05M AA reduction step was replaced by reduction in 0.05M hydrazine. The capacitance between AA and hydrazine reduction were very similar and no conclusive trend could be drawn.[64] Therefore hydrazine reduction was excluded herein.

## 4.3 Coin Cell Assembly

The as-prepared rGO/N was soaked in 2M KOH overnight to ensure thorough penetration of the electrolyte throughout the porous electrode.



Bottom Cover   rGO/N Electrode   Paper Separator   rGO/N Electrode   Current Collector   Spacer   Top Cover

**Figure 24. Components for Coin Cell Assembly**

Figure 24 shows the array of components that comprise the symmetrical coin cell supercapacitor. It was assembled by stacking each component starting from the bottom cover, electrode, Whatman #4 filter paper, electrode, current collector, spacer, and top cover. KOH (2M, 1 ml) was added atop the paper separator to ensure sufficient electrolyte was present within the coin cell. Post assembly, the coin cell was hand-crimped to provide adequate pressure for contact.

Since the pressure was directly correlated to the capacitance retention, it was qualitatively investigated. The pressure was qualitatively assessed by estimating the inward bulge generated by crimping. The following scenarios were prepared for this evaluation: electrode was lightly crimped (no bulge),

moderately crimped (slight bulge) and excessively crimped (would not bulge further). Results showed that excess crimping yielded up to 40% increased capacitance performance, most likely due to closer contact of components. For all successive coin cell assemblies, the coin cell was excessively crimped.

## 4.4 Characterizations

The materials were characterized via multiple techniques. Scanning electron microscopy (SEM, Zeiss Ultra Plus Field SEM), and transmission electron microscopy (TEM, JEOL 2010F) were used to examine the foam morphology and the approximate size distributions of the graphene sheets. X-ray diffraction (XRD, Bruker-AXS D8 Discover diffractometer) and Raman spectroscopy (Bruker Senterra, 532nm) were used to evaluate the GO and graphene crystal structures and surface defects. GO and graphene were scraped off and collected from pre- and post- reduction of the coin cells for nanoscopic imaging and compositional analysis. Surface area was investigated with a UV-Visible Spectrometer (UV-Vis, Fisher Scientific GENESYS 10S) via methylene blue (peak at 661nm) as the active adsorbent.

Electrochemical measurements, such as cyclic voltammetry (CV), galvanostatic charge/discharge (GCD), and electrical impedance spectroscopy (EIS) were performed using a Versastat MC Potentiostat from Princeton Applied Research. The potential difference of interest is between 0 to 1V for CV and GCD. EIS was measured at frequencies between 10 mHz to 200 kHz to with a sinusoidal signal amplitude of 10mV RMS. Electrochemical characterization equations used to interpret and analyze results was previously discussed in the Section 3.2.

# 5.0 Results and Discussion

## 5.1 Structure and Morphology
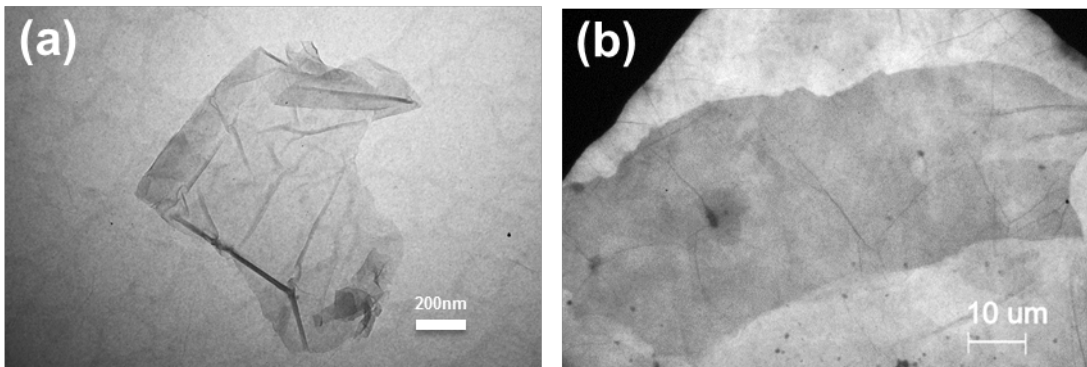


**Figure 25.TEM images of (a) s-GO and (b) L-GO**

Figure 25 (a, b) shows representative TEM images of GO synthesized from (a) s-graphite and (b) L-graphite. The figure demonstrates the notable wrinkled nanoplatelet texture, characteristic of single or few layered graphene sheets. Here, the harsh oxidation of graphite has significantly reduced its original grain size. The representative planar lengths of GO sheets were approximately 80 μm and 1 μm, compared to their initial corresponding starting 800 μm and 10 μm graphite particle size (Figure 25 (a) and Figure 25 (b) for s-GO and L-GO respectively). This confirms that L-GO, which was synthesized from L-graphite, maintains its superior planar dimensions over s-GO, of which were prepared from s-graphite. It should be noted that for L-GO, in Figure 25 (b), a smaller GO sheet was selected as the appropriate image because majority of the GO sheets exceeded the TEM grid (200 mesh).
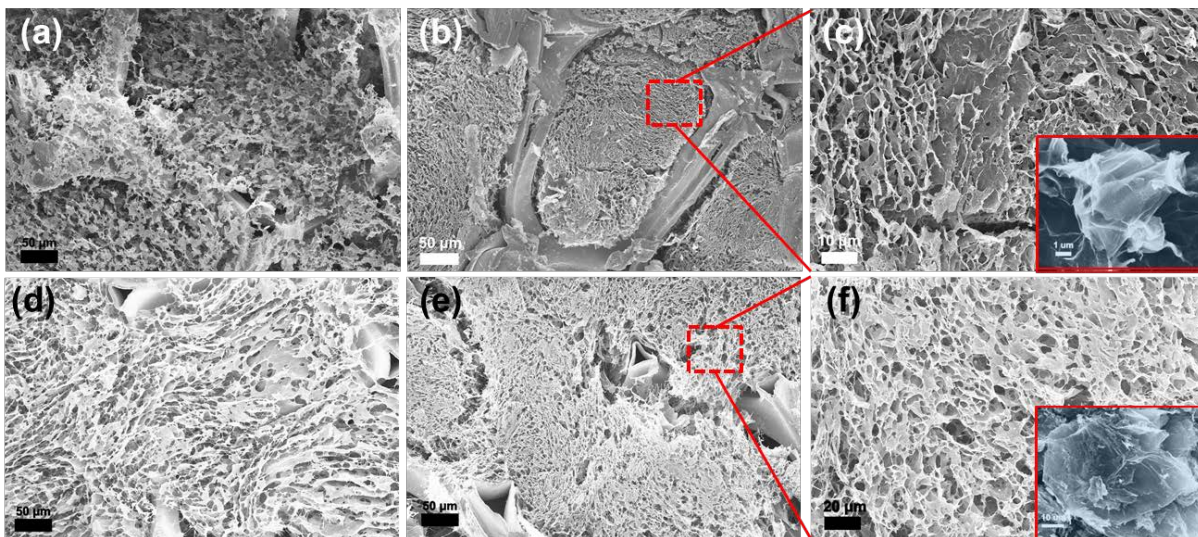
**Figure 26. SEM images of (a) s-GO/N, (b) s-rGO/N, (c) magnification of s-rGO/N along with isolated rGO (inset). (d) L-GO/N, (e) L-rGO/N, and (f) magnification of L-rGO/N with isolated rGO (inset).**

Representative scanning electron microscopy (SEM) images of GO foam and graphene foam covering the surface of porous nickel are shown in Figure 26. The crumpled morphology remained evident throughout the process, confirming the presence of GO and was preserved when reduced to rGO. Post-reduction, the rGO sheets continued to maintain an approximate average of 1 μm and 70 μm for s-rGO and L-rGO respectively. This affirms that the chemical reduction did not significantly reduce the planar size of graphene sheets; however, the rGO sheets in L-rGO remained larger than that of s-rGO. While GO generally tends to agglomerate, the SEM images display the porous foam architecture preventing such phenomenon from materializing, and thereby able to maintain a high effective surface area for electrostatic accumulation. The pores average a diameter of 2 μm for s-rGO (Figure 26(b, c)) while averaging a diameter of 8 μm for L-rGO (Figure 26 (e, f)). The smaller yet more abundant pores found in s-rGO will increase the effective surface area, and understandably contribute to the superior capacitance in contrast to L-rGO. In addition, the presence of the nickel scaffold acts as a macro-spacer to prevent

macro-aggregation (Figure 26 (e, f)).[40, 65, 66] In Figure 26 (e-h), the higher magnification further confirms

the L-rGO still maintains its significantly larger sheet size over that of s-rGO.

Using methylene blue adsorption, the surface area of L-rGO and s-rGO were averaged to 72 $m^2$/g and 154

$m^2$/g respectively. We have noticed that these values are lower than literature-reported surface areas

evaluated from BET analysis for graphene foam.[37] Nonetheless, this confirms that rGO with smaller

planar sheet sizes have a larger surface areas than L-rGO, which entails that smaller graphene sheets

should be able to retain more capacitance.
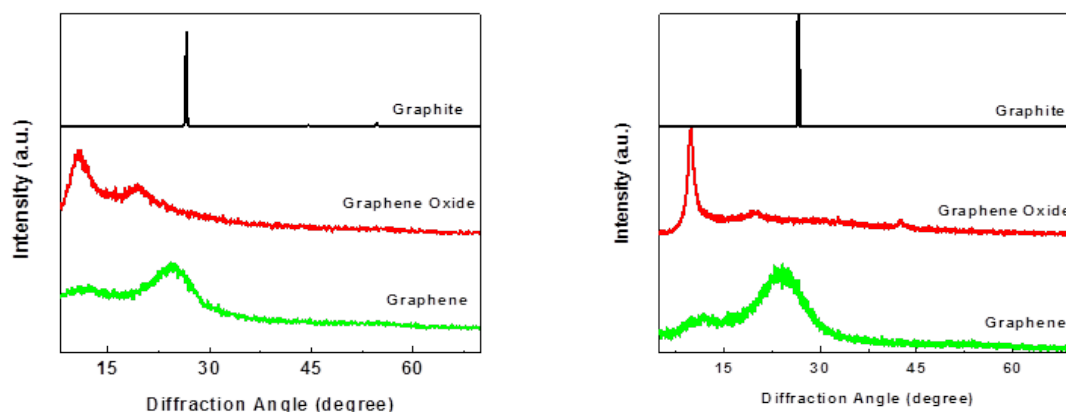


**Figure 27. XRD of (a) s-graphite, s-GO, s-rGO and (b) L-graphite, L-GO, and L-rGO respectively**

**Table 2. Table of values obtained from XRD**

| | | 2θ (degree) | d-spacing (Å) | FWHM (2θ) | FWHM (radian) | $L_c$ (Å) | # of Layers |
|---|---|---|---|---|---|---|---|
| s- | Graphite | 26.54 | 3.36 | 0.19657 | 0.00172 | 830.45 | 247.51 |
| | GO | 10.57 | 8.37 | 10.24529 | 0.08941 | 15.57 | 1.86 |
| | rGO | 24.72 | 3.60 | 13.03187 | 0.11372 | 12.48 | 3.47 |
| L- | Graphite | 26.57 | 3.35 | 0.28191 | 0.00246 | 579.09 | 172.78 |
| | GO | 9.96 | 8.88 | 8.4352 | 0.07361 | 18.91 | 2.13 |
| | rGO | 24.14 | 3.68 | 10.03184 | 0.08754 | 16.20 | 4.40 |

Figure 22 displays the XRD results of small graphite and large graphite derived GO and graphene. The

list of parameters calculated from XRD measurements are compiled in Table 2. Both graphite sources

display a major (002) peak at 26.55±0.02, which corresponds to an inter-sheet distance of 3.36±0.01 Å (calculated from Equation 1). Upon oxidation, the (002) peaks shifts to 10.27±31, which translates to an average interlayer spacing of 8.12±0.77Å.[67] Finally, post-reduction, the (002) reverts back to 24.43±0.29, corresponding to a d-spacing of 3.64±0.04 Å.[67] This restoration confirms the partial recovery the graphitic crystal structure and partial restacking as shown by the slight increase in the number of layers (Equation 3).[63] For both sizes of graphene-based samples, the crystallite size significantly drops upon oxidation, and further drops in size when reduced. Additionally, the reduction of graphene oxide induced the removal of oxygen functional groups from the basal plane, resulting in the observed decrease in d-spacing.[39] The number of layers The XRD patterns affirm that GO and rGO were successfully prepared.
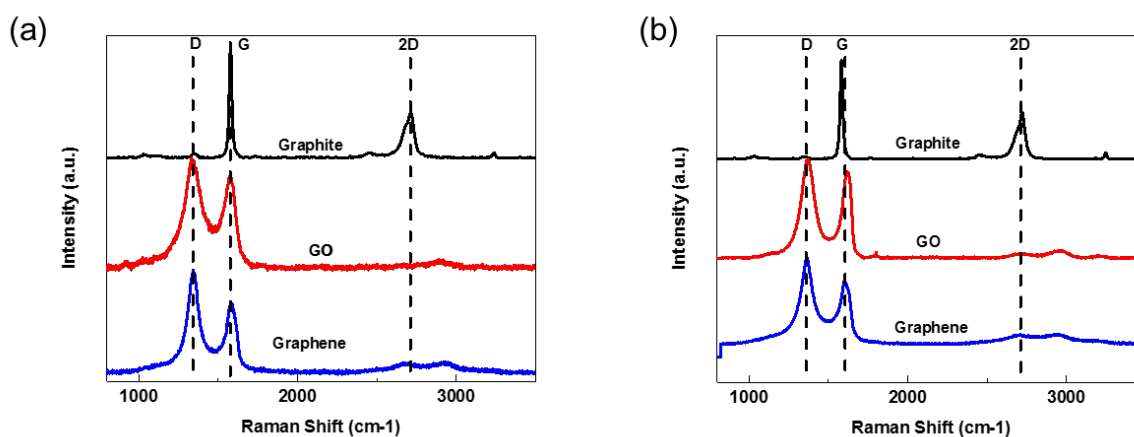


**Figure 28. Raman of (a) s-graphite, s-GO, s-rGO and (b) L-graphite, L-GO, and L-rGO respectively**

**Table 3. Parameters calculated from Raman Spectra**

| Size | | D-Band (cm$^{-1}$) | G-Band (cm$^{-1}$) | $I_D/I_G$ | $I_{2D}/I_G$ | $L_a$, nm |
|---|---|---|---|---|---|---|
| s- | Graphite | 1344.5 | 1578.1 | 0.04 | 0.40 | 478.13 |
| | GO | 1332.9 | 1572.6 | 1.20 | 0.05 | 16.32 |
| | Graphene | 1344.1 | 1577.9 | 1.40 | 0.23 | 13.95 |
| L- | Graphite | 1349.2 | 1582.4 | 0.03 | 0.49 | 676.46 |
| | GO | 1350.7 | 1595.0 | 1.15 | 0.06 | 17.03 |
| | Graphene | 1347.3 | 1581.3 | 1.29 | 0.30 | 15.09 |

Figure 28 compares the Raman spectra of graphite, GO and rGO prepared from s-graphite and L-graphite respectively. The properties of interest for the different materials are summarized in Table 3. The spectra displays the prominent D, G, and 2D peaks for graphite, GO, and graphene of both sheet sizes. Upon oxidation, the D-band begins to dominate indicating a reduction in the size of in-plane sp$^2$ domains. The increase of $I_D/I_G$ post-reduction, reveals that although the chemical reduction may have partially restored some of the sp$^2$ planar configurations, new smaller conjugated domains may have been created in addition to the domains present before reduction.[37, 64] In addition, the higher $I_D/I_G$ found in the s-Graphite/s-GO/s-rGO samples in comparison to L-Graphite,/L-GO,/L-rGO indicates that the smaller sheets also possess a smaller average size of crystalline domains, implying more edge defects.[64] This could mean that the increased defect concentration also decreases the electrical conductivity of graphene due to greater amounts of disturbances in the sp$^2$ network, but results in higher ion binding to the electrolyte.[40] $I_{2D}/I_G$ values, which are proportional to charge carrier concentration[39], are also listed in Table 3. These values imply that the materials ordered from most to least conductive are: graphite, graphene then graphene oxide. Practically, L-rGO possesses marginally higher electrical conductivity than s-rGO. The $I_D/I_G$ ratios and the corresponding results of $L_a$ are also compiled (Table 3). The larger $L_a$ value found with L-rGO implies that there are fewer edge defects, which resulted in an increased electrical conductivity.[68] To conclude, from the Raman spectra, we expect that the graphene with larger planar sheets will have

superior electrical conductivity over graphene with smaller planar sheets due to the lower $I_D/I_G$ ratio, higher $I_{2D}/I_G$ ratio and larger $L_a$. Small-size graphene, although having lower conductivity, could also lead to higher ion binding and ion wettability.

## 5.2 Electrochemical Performance

### 5.2.1 Comparison based on Graphite Size
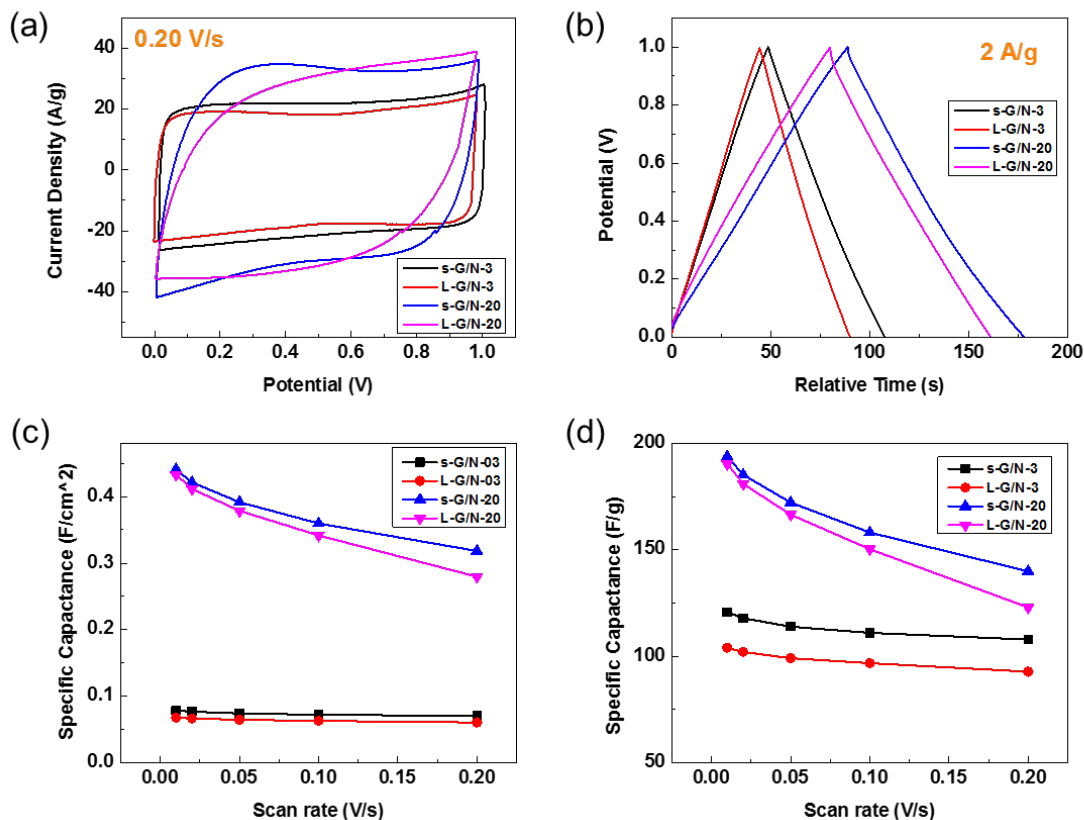


**Figure 29. Graphs of specific capacitance contrasting s-rGO/N-3, L-rGO/N-3, s-rGO/N-20, L-rGO/N-20 from (a) CV at a scan rate of 0.20V/s. (b) GCD at 2 A/g. Specific capacitance summary normalized by (c) area and (d) mass, calculated from CV.**

Figure 29 compares the electrochemical properties amongst s-rGO/N-3, s-rGO/N-20, L-rGO/N-3, and L-rGO/N-20. Figure 29 consistently displays s-rGO/N-3 and s-rGO/N-20 exhibiting noticeably higher capacitance than L-rGO/N-3 and L-rGO/N-20 respectively. The resulting gravimetric capacitance at 10 mV/s peaked at 194 F/g and 190 F/g for s-rGO/N-20 and L- rGO /N-20 respectively.  It is also important to note that the capacitance from the nickel foam here is negligible.[69] Figure 29 (a) shows the CV curves

are essentially rectangular at 3 mg/mL, however, slight deformations are manifested at 20 mg/mL. The deformation is more defined with L-rGO/N-20, which is likely due to the partial filling of pores within the rGO network (in Figure 26) as the concentration of GO increases, resulting in greater ionic diffusion resistance. From the practically rectangular shape of the CV curve, we can safely assume that the capacitance solely originates from electrostatic accumulation (as opposed to pseudocapacitance). Thus, we can infer that the improved 3-16% capacitance is due to the slightly larger surface area manifested in smaller particles (compared to larger particles) within a given volume. Figure 29 (b) presents EDLC characteristics that are evident from the linearity and symmetry noted in the GCD curves. Figure 5 (c, d) demonstrates the capacitance superiority exhibited in s-rGO/N against L-rGO/N regardless of scan rate.
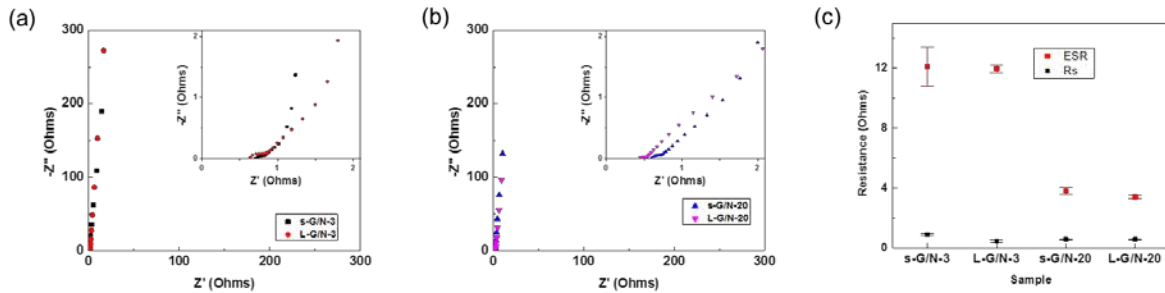


**Figure 30. (a, b) Nyquist plots comparing s-rGO-3, S-rGO-20, L-rGO-3, and L-rGO-20. (c) Compares the various ESR and RS in graphical form.**

Figure 30 (a, b) presents the Nyquist plots for the corresponding cells. At the high frequency, the $R_S$ is depicted graphically as the first x-intercept on the Nyquist plot.[7] With all other conditions kept virtually constant, any divergence between $R_S$ values can be connected to the influence from the inherent different planar sizes. The $R_S$ values of L-rGO/N-3 and L-rGO/N-20 are 20–48% greater than that of s-rGO/N-3 and s-rGO/N-20 respectively, which implies that rGO with larger planar sheets are less resistive than rGO comprised of smaller sheets. The lower resistance observed in larger sheets is probably due to fewer surface defects and potentially larger $sp^2$ domains (observed in Figure 28) that enabled more efficient

electron transfer. However, as the frequency decreases the impedance behaviour depicts a semi-circle, which is often correlated to the charge transfer resistance.[7] In Figure 30 (a, b), L-rGO/N-3 and L-rGO/N-20 exhibit wider semi-circles than s-rGO/N-3 and s-rGO/N-20, respectively. This is also presumably because of a higher ionic wettability, which is associated with the larger surface defect ratio (Figure 28) found in graphene with smaller sheets.[70] Further decreasing the frequency, the impedance plot shifts to a visible knee frequency followed by a 45° phase angle. This can be described by the Warburg element and is characteristic of the transition from frequency dependent diffusion to capacitive charging behaviour.[11] It is also observed in Figure 30(a, b) that as the sheet size increases, this transition also increases, which translates to a higher ion diffusion resistance. This slightly higher diffusion resistance observed in graphene with larger sheets matches the behaviour noted in the rectangularity of the cyclic voltammetry (Figure 29(a)), which we previously attributed to the increased blockage of pores.

The ESR values calculated from the IR drop of GCD (Figure 29 (b)) are larger in the s-rGO/N than their corresponding L-rGO/N. As observed (Figure 30 (c)), the ESR decreases slightly as the size of graphene sheets increase. Although L-rGO exhibit greater diffusion resistance, the intrinsic resistance of s-rGO compensates, still resulting in a larger overall ESR (Figure 30 (c)). Therefore, as a standalone electrode material, rGO with smaller sheet sizes have 3-16% superior capacitance, whereas rGO with larger sheets have a lower intrinsic and overall resistance when compared to rGO with smaller planar sheets.
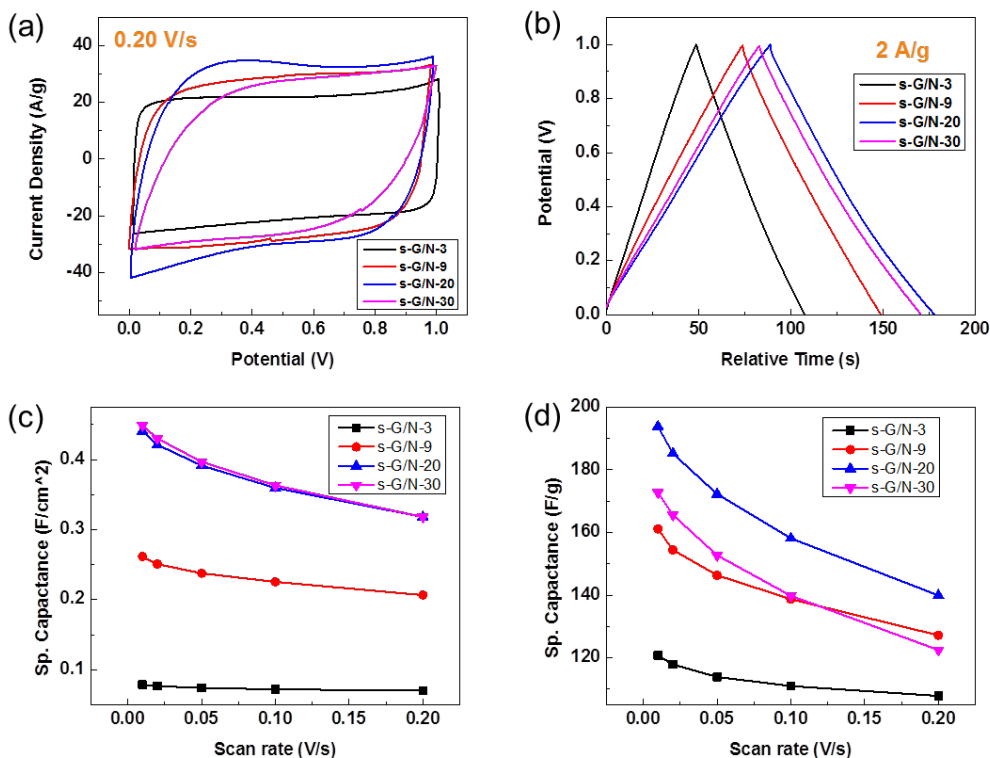
**Figure 31. Graphs of specific capacitance contrasting s-rGO/N-3, L-rGO/N-3, s-rGO/N-20, L-rGO/N-20 from (a) CV at a scan rate of 0.20V/s.  (b) GCD at 2 A/g. Specific capacitance summary normalized by (c) area and (d) mass, calculated from CV.**

Figure 31 compares the electrochemical properties of the s-rGO/N at different loadings. A trend is observed in Figure 31, whereby increasing the precursor concentration from 3 mg/mL to 20 mg/mL results in an increase of the areal and gravimetric capacitance. However, further increase in the GO precursor concentration results in an insignificant change to the areal capacitance and even a decrease in the gravimetric capacitance. The resulting gravimetric capacitance at 10 mV/s, ranged from 120.7 F/g to 194 F/g for s-rGO/N (Figure 31 (c)). Since the GO concentration is proportionally related to the graphene loading on the nickel foam, we speculate that this decreased gravimetric capacitance is due to the decreased utilization of the effective surface area for EDL formation when increasing the GO

54

concentration over 20 mg/mL. Figure 31(a) displays the CV of all the loadings operated at a scan rate of 0.20 V/s. The CV curves are virtually rectangular at 3mg/mL, showing that an approach to ideal and reversible capacitive behavior is almost achieved. However, as the GO concentration increases, the CV shape begins to deviate further away from the rectangular shape. We believe this is due to excess amounts of rGO within the porous nickel, which began to hinder ion diffusivity, as reflected in the EIS analysis. Figure 31(b) shows the CD curves obtained at a current density of 2 A/g between 0 V and 1 V in 2 M KOH. The GCD (Figure 31 (b)) further confirm the capacitance trends previously observed in CV (Figure 31 (a)).
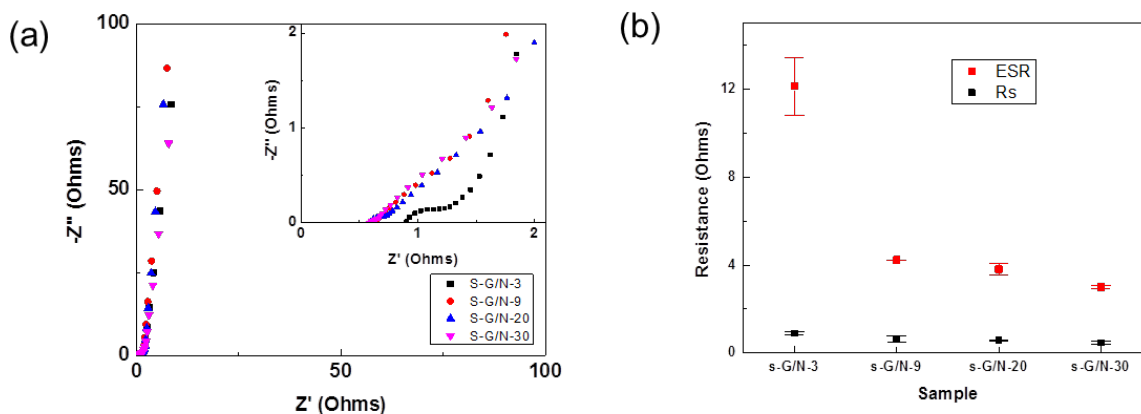


**Figure 32. (a) Nyquist plot comparing the various loadings of s-rGO/N. (b) Compares the various ESR and $R_S$ in graphical form.**

Figure 32(b) graphically summarizes the $R_S$ and ESR at each loading. The ESR decreases as the density of graphene increases on the nickel foam. This decreasing ESR is probably due to the increased presence of rGO made available for facilitating electron transfer and decreasing the charge transfer resistance within the electrode. Hence, increasing the GO concentration precursor increases capacitance and decreases the resistance. In this study, the capacitance was optimized at 194 F/g with a GO concentration of 20 mg/mL.

# 5.0 Conclusions and Future Direction

In summary, rGO was impregnated into porous nickel via the facile dip-coating technique. GO solutions were prepared by varying the precursor graphite sources as well as the concentrations. Utilizing the coin cell setup, the capacitance and resistance were evaluated and a correlation linking back to the planar size of graphene was established. As such, this thesis fulfills the original objective of elucidating the relationship between graphene planar sizes and capacitance in supercapacitor application. Additionally, mass loadings were also investigated and optimized.

L-graphite and s-graphite were used to prepare GO solutions of various concentrations. Porous nickel was saturated with this GO solution, and then chemically reduced prior to lyophilisation to prepare graphene foam in nickel foam. s-rGO/N that originated from s-graphite exhibited a capacitance of up to 194 F/g, of which outperformed L-rGO/N, which originated from L-graphite, at 190 F/g. The GO concentration used to make these electrodes, correlated directly to the end mass loading, however, L-rGO exhibited marginally lower intrinsic and overall resistance than s-rGO. However, s-rGO possessed greater surface area, improved ionic wettability and lesser diffusion resistance, ultimately retaining more charge than L-rGO. Moreover, 20 mg/mL was found to be the optimal concentration for s-rGO/N to maximize gravimetric capacitance. This study reveals that rGO synthesized from graphite with smaller particle sizes are more suitable as a standalone electro-active material, whereas rGO generated from graphite with larger particle size would be more suitable as a conductive scaffold for the deposition of other electro-active materials within the application of supercapacitors.

Despite elucidating the relationship between graphene planar sizes and its role in supercapacitors, additional work should be made to further verify this trend. Based on the results of the current work, the following future work is recommended:

I. Fractionation of GO: Extra steps should be inserted to fractionate the graphene oxide based on sheet size.[71] In addition, size distributions should be quantified via dilute GO solutions via either SEM or TEM. This will allow at least three different size distributions of graphene planar sizes, which will increase the reliability of the data.

II. Supercapacitor electrode: It would be worth investigating whether the pores within the rGO foam can be coated with a redox-active material to boost the performance of the supercapacitors.

III. Electrode/electrolyte compatibility: It is quite important for maximizing the potential within any given supercapacitor. Thus, another venue that should be considered is preparing GO functionalized membranes as solid or liquid electrolyte.

# References

1.      SourceOECD. *World energy outlook*; OECD/IEA2013.

2.      Becker, H. I. Low voltage electrolytic capacitor. USA Patent 1957.

3.      Robinett, M. I.; Snyder, D. Rechargeable portable light with multiple charging systems. USA

Patent 2003.

4.      Ridden, P. Helium Bluetooth speakers powered by supercapacitors.

http://www.gizmag.com/helium-capacitor-powered-speakers/29938/ (accessed July 20).

5.      White, C. Coleman FlashCell Cordless Screwdriver Charges in 90 Seconds.

http://gizmodo.com/305713/coleman-flashcell-cordless-screwdriver-charges-in-90-seconds (accessed

July 20).

6.      International, S. Mazda introduces supercapacitor-type regenerative braking. *Automotive*

*Engineering magazine*, 2013.

7.      Kang, J.; Wen, J.; Jayaram, S. H.; Yu, A.; Wang, X. Development of an equivalent circuit model for

electrochemical double layer capacitors (EDLCs) with distinct electrolytes. *Electrochimica Acta* **2014,** *115*,

587-598.

8.      Li, H.; Peng, J.; Liu, W.; Huang, Z. Stationary Charging Station Design for Sustainable Urban Rail

Systems: A Case Study at Zhuzhou Electric Locomotive Co., China. *Sustainability* **2015,** *7* (1), 465-481.

9.      Zhong, C.; Deng, Y.; Hu, W.; Qiao, J.; Zhang, L.; Zhang, J. A review of electrolyte materials and

compositions for electrochemical supercapacitors. *Chemical Society Reviews* **2015**.

10.      Yuan, A.; Zhang, Q. A novel hybrid manganese dioxide/activated carbon supercapacitor using

lithium hydroxide electrolyte. *Electrochemistry Communications* **2006,** *8* (7), 1173-1178.

11.      Conway, B. E. *Electrochemical supercapacitors: scientific fundamentals and technological*

*applications*; Springer Science & Business Media2013.

12.      Zheng, J.; Cygan, P.; Jow, T. Hydrous ruthenium oxide as an electrode material for electrochemical capacitors. *Journal of the Electrochemical Society* **1995,** *142* (8), 2699-2703.

13.      Wei, W.; Cui, X.; Chen, W.; Ivey, D. G. Manganese oxide-based materials as electrochemical supercapacitor electrodes. *Chemical Society Reviews* **2011,** *40* (3), 1697-1721.

14.      Davies, A.; Audette, P.; Farrow, B.; Hassan, F.; Chen, Z.; Choi, J.-Y.; Yu, A. Graphene-based flexible supercapacitors: pulse-electropolymerization of polypyrrole on free-standing graphene films. *The Journal of Physical Chemistry C* **2011,** *115* (35), 17612-17620.

15.      Mastragostino, M.; Arbizzani, C.; Soavi, F. Conducting polymers as electrode materials in supercapacitors. *Solid state ionics* **2002,** *148* (3), 493-498.

16.      Bacon, M.; Bradley, S. J.; Nann, T. Graphene quantum dots. *Particle & Particle Systems Characterization* **2014,** *31* (4), 415-428.

17.      Nobelprize.org. The Nobel Prize in Physics 2010. http://www.nobelprize.org/nobel_prizes/physics/laureates/2010/ (accessed 18/07/2015).

18.       Chen, D.; Tang, L.; Li, J. Graphene-based materials in electrochemistry. *Chemical Society Reviews* **2010,** *39* (8), 3157-3180.

19.      Bonaccorso, F.; Colombo, L.; Yu, G.; Stoller, M.; Tozzini, V.; Ferrari, A. C.; Ruoff, R. S.; Pellegrini, V. Graphene, related two-dimensional crystals, and hybrid systems for energy conversion and storage. *Science* **2015,** *347* (6217), 1246501.

20.       Hummers Jr, W. S.; Offeman, R. E. Preparation of graphitic oxide. *Journal of the American Chemical Society* **1958,** *80* (6), 1339-1339.

21.      Chakrabarti, A.; Lu, J.; Skrabutenas, J. C.; Xu, T.; Xiao, Z.; Maguire, J. A.; Hosmane, N. S. Conversion of carbon dioxide to few-layer graphene. *Journal of Materials Chemistry* **2011,** *21* (26), 9491-9493.

22.     Kim, K. S.; Zhao, Y.; Jang, H.; Lee, S. Y.; Kim, J. M.; Kim, K. S.; Ahn, J.-H.; Kim, P.; Choi, J.-Y.; Hong, B. H. Large-scale pattern growth of graphene films for stretchable transparent electrodes. *Nature* **2009,** *457* (7230), 706-710.

23.     Marcano, D. C.; Kosynkin, D. V.; Berlin, J. M.; Sinitskii, A.; Sun, Z.; Slesarev, A.; Alemany, L. B.; Lu, W.; Tour, J. M. Improved synthesis of graphene oxide. *ACS nano* **2010,** *4* (8), 4806-4814.

24.     Brodie, B. C. On the atomic weight of graphite. *Philosophical Transactions of the Royal Society of London* **1859**, 249-259.

25.     Staudenmaier, L. Method for the preparation of graphitic acid. *Ber Dtsch Chem Ges* **1898,** *31*, 1481-1487.

26.     Dreyer, D. R.; Park, S.; Bielawski, C. W.; Ruoff, R. S. The chemistry of graphene oxide. *Chemical Society Reviews* **2010,** *39* (1), 228-240.

27.     He, H.; Riedl, T.; Lerf, A.; Klinowski, J. Solid-state NMR studies of the structure of graphite oxide. *The Journal of physical chemistry* **1996,** *100* (51), 19954-19958.

28.     Ding, Y.; Zhang, P.; Zhuo, Q.; Ren, H.; Yang, Z.; Jiang, Y. A green approach to the synthesis of reduced graphene oxide nanosheets under UV irradiation. *Nanotechnology* **2011,** *22* (21), 215601.

29.     Zhu, Y.; Murali, S.; Stoller, M. D.; Velamakanni, A.; Piner, R. D.; Ruoff, R. S. Microwave assisted exfoliation and reduction of graphite oxide for ultracapacitors. *Carbon* **2010,** *48* (7), 2118-2122.

30.     Jeong, H.; Jin, M.; So, K.; Lim, S.; Lee, Y. Tailoring the characteristics of graphite oxides by different oxidation times. *Journal of Physics D: Applied Physics* **2009,** *42* (6), 065418.

31.     Stankovich, S.; Dikin, D. A.; Piner, R. D.; Kohlhaas, K. A.; Kleinhammes, A.; Jia, Y.; Wu, Y.; Nguyen, S. T.; Ruoff, R. S. Synthesis of graphene-based nanosheets via chemical reduction of exfoliated graphite oxide. *Carbon* **2007,** *45* (7), 1558-1565.

32.     Zhang, J.; Yang, H.; Shen, G.; Cheng, P.; Zhang, J.; Guo, S. Reduction of graphene oxide via L-ascorbic acid. *Chemical Communications* **2010,** *46* (7), 1112-1114.

33.	Lei, Z.; Lu, L.; Zhao, X. The electrocapacitive properties of graphene oxide reduced by urea.

*Energy & Environmental Science* **2012,** *5* (4), 6391-6399.

34.	Shin, H. J.; Kim, K. K.; Benayad, A.; Yoon, S. M.; Park, H. K.; Jung, I. S.; Jin, M. H.; Jeong, H. K.; Kim,

J. M.; Choi, J. Y. Efficient reduction of graphite oxide by sodium borohydride and its effect on electrical

conductance. *Advanced Functional Materials* **2009,** *19* (12), 1987-1992.

35.	Moon, I. K.; Lee, J.; Ruoff, R. S.; Lee, H. Reduced graphene oxide by chemical graphitization.

*Nature communications* **2010,** *1*, 73.

36.	Fan, X.; Peng, W.; Li, Y.; Li, X.; Wang, S.; Zhang, G.; Zhang, F. Deoxygenation of exfoliated

graphite oxide under alkaline conditions: a green route to graphene preparation. *Advanced Materials*

**2008,** *20* (23), 4490-4493.

37.	Chen, J.; Sheng, K.; Luo, P.; Li, C.; Shi, G. Graphene Hydrogels Deposited in Nickel Foams for

High‐Rate Electrochemical Capacitors. *Advanced Materials* **2012,** *24* (33), 4569-4573.

38.	Chen, M.; Liu, J.; Chao, D.; Wang, J.; Yin, J.; Lin, J.; Fan, H. J.; Shen, Z. X. Porous α-Fe 2 O 3

nanorods supported on carbon nanotubes-graphene foam as superior anode for lithium ion batteries.

*Nano Energy* **2014,** *9*, 364-372.

39.	Hassan, F. M.; Chabot, V.; Li, J.; Kim, B. K.; Ricardez-Sandoval, L.; Yu, A. Pyrrolic-structure

enriched nitrogen doped graphene for highly efficient next generation supercapacitors. *Journal of*

*Materials Chemistry A* **2013,** *1* (8), 2904-2912.

40.	Kim, N. H.; Kuila, T.; Lee, J. H. Simultaneous reduction, functionalization and stitching of

graphene oxide with ethylenediamine for composites application. *Journal of Materials Chemistry A* **2013,**

*1* (4), 1349-1358.

41.	Allen, M. J.; Tung, V. C.; Kaner, R. B. Honeycomb carbon: a review of graphene. *Chemical reviews*

**2009,** *110* (1), 132-145.

42.	Bointon, T. H.; Barnes, M. D.; Russo, S.; Craciun, M. F. High Quality Monolayer Graphene Synthesized by Resistive Heating Cold Wall Chemical Vapor Deposition. *Advanced Materials* **2015,** *27* (28), 4200-4206.

43.	Babenko, V.; Murdock, A. T.; Koos, A. A.; Britton, J.; Crossley, A.; Holdway, P.; Moffat, J.; Huang, J.; Alexander-Webber, J. A.; Nicholas, R. J.; Grobert, N. Rapid epitaxy-free graphene synthesis on silicidated polycrystalline platinum. *Nat Commun* **2015,** *6*.

44.	Goldstein, J.; Newbury, D. E.; Joy, D.; Lyman, C.; Echlin, P.; Lifshin, E.; Sawyer, L.; Michael, J. Scanning electron microscopy and x-ray microanalysis. 2003. *ISBN 306472929*, 9780306472923.

45.	L. Reimer, H. K. *Transmission electron microscopy: physics of image formation*; 5th ed.; Springer2008; Vol. 36.

46.	Connolly, J. R. Introduction to X-ray powder diffraction. *European Physical Society of Journal* **2007,** *4*, p400.

47.	Langford, J. I.; Wilson, A. Scherrer after sixty years: a survey and some new results in the determination of crystallite size. *Journal of Applied Crystallography* **1978,** *11* (2), 102-113.

48.	Brunauer, S.; Emmett, P. H.; Teller, E. Adsorption of gases in multimolecular layers. *Journal of the American Chemical Society* **1938,** *60* (2), 309-319.

49.	Misra, P.; Dubinskii, M. A. *Ultraviolet spectroscopy and UV lasers*; CRC Press2002.

50.	Liu, T.; Li, Y.; Du, Q.; Sun, J.; Jiao, Y.; Yang, G.; Wang, Z.; Xia, Y.; Zhang, W.; Wang, K. Adsorption of methylene blue from aqueous solution by graphene. *Colloids and Surfaces B: Biointerfaces* **2012,** *90*, 197-203.

51.	McAllister, M. J.; Li, J.-L.; Adamson, D. H.; Schniepp, H. C.; Abdala, A. A.; Liu, J.; Herrera-Alonso, M.; Milius, D. L.; Car, R.; Prud'homme, R. K. Single sheet functionalized graphene by oxidation and thermal expansion of graphite. *Chemistry of Materials* **2007,** *19* (18), 4396-4404.

52.     Ferrari, A. C.; Basko, D. M. Raman spectroscopy as a versatile tool for studying the properties of graphene. *Nature nanotechnology* **2013,** *8* (4), 235-246.

53.     Vandenabeele, P. *Practical Raman spectroscopy: an introduction*; John Wiley & Sons2013.

54.     Cancado, L.; Takai, K.; Enoki, T.; Endo, M.; Kim, Y.; Mizusaki, H.; Jorio, A.; Coelho, L.; Magalhaes-Paniago, R.; Pimenta, M. General equation for the determination of the crystallite size La of nanographite by Raman spectroscopy. *Applied Physics Letters* **2006,** *88* (16), 163106-163106.

55.     Research, P. A. *A Review of Techniques for Electrochemical Analysis*; Application Note; Princeton Applied Research: Oak Ridge, TN, USA2010.

56.     Research, P. A. *Subject: A review of Techniques for Electrochemical Analysis*; Application Note; Princeton Applied Research 801 S. Illinois Avenue, Oak Ridge, TN 378302014.

57.     Stoller, M. D.; Ruoff, R. S. Best practice methods for determining an electrode material's performance for ultracapacitors. *Energy & Environmental Science* **2010,** *3* (9), 1294-1301.

58.     Kalnaus, S.; Rhodes, K.; Daniel, C. A study of lithium ion intercalation induced fracture of silicon particles used as anode material in Li-ion battery. *Journal of Power Sources* **2011,** *196* (19), 8116-8124.

59.     Instruments, G. *Basics of Electrochemical Impdeance Spectroscopy*; AppliationNOTE; Gamry Instruments: 734 Louis Drive, Warminister, PA, USA2010, p 17.

60.     Dimiev, A. M.; Tour, J. M. Mechanism of graphene oxide formation. *ACS nano* **2014,** *8* (3), 3060-3068.

61.     Li, J.-L.; Kudin, K. N.; McAllister, M. J.; Prud'homme, R. K.; Aksay, I. A.; Car, R. Oxygen-driven unzipping of graphitic materials. *Physical review letters* **2006,** *96* (17), 176101.

62.     Yu, A.; Ramesh, P.; Itkis, M. E.; Bekyarova, E.; Haddon, R. C. Graphite nanoplatelet-epoxy composite thermal interface materials. *The Journal of Physical Chemistry C* **2007,** *111* (21), 7565-7569.

63.	Long, D.; Li, W.; Ling, L.; Miyawaki, J.; Mochida, I.; Yoon, S.-H. Preparation of nitrogen-doped graphene sheets by a combined chemical and hydrothermal reduction of graphene oxide. *Langmuir* **2010,** *26* (20), 16096-16102.

64.	Wang, H.; Robinson, J. T.; Li, X.; Dai, H. Solvothermal reduction of chemically exfoliated graphene sheets. *Journal of the American Chemical Society* **2009,** *131* (29), 9910-9911.

65.	Ye, S.; Feng, J.; Wu, P. Deposition of three-dimensional graphene aerogel on nickel foam as a binder-free supercapacitor electrode. *ACS applied materials & interfaces* **2013,** *5* (15), 7122-7129.

66.	Xu, C.; Li, J.; Wang, X.; Wang, J.; Wan, L.; Li, Y.; Zhang, M.; Shang, X.; Yang, Y. Synthesis of hemin functionalized graphene and its application as a counter electrode in dye-sensitized solar cells. *Materials Chemistry and Physics* **2012,** *132* (2), 858-864.

67.	Naebe, M.; Wang, J.; Amini, A.; Khayyam, H.; Hameed, N.; Li, L. H.; Chen, Y.; Fox, B. Mechanical Property and Structure of Covalent Functionalised Graphene/Epoxy Nanocomposites. *Sci. Rep.* **2014,** *4*.

68.	Lin, X.; Shen, X.; Zheng, Q.; Yousefi, N.; Ye, L.; Mai, Y.-W.; Kim, J.-K. Fabrication of highly-aligned, conductive, and strong graphene papers using ultralarge graphene oxide sheets. *ACS nano* **2012,** *6* (12), 10708-10719.

69.	Zhao, Y.-Q.; Zhao, D.-D.; Tang, P.-Y.; Wang, Y.-M.; Xu, C.-L.; Li, H.-L. MnO< sub>2</sub>/graphene/nickel foam composite as high performance supercapacitor electrode via a facile electrochemical deposition strategy. *Materials Letters* **2012,** *76*, 127-130.

70.	Pandolfo, A.; Hollenkamp, A. Carbon properties and their role in supercapacitors. *Journal of power sources* **2006,** *157* (1), 11-27.

71.	Chen, J.; Li, Y.; Huang, L.; Jia, N.; Li, C.; Shi, G. Size Fractionation of Graphene Oxide Sheets via Filtration through Track-Etched Membranes. *Advanced Materials* **2015,** *27* (24), 3654-3660.